AFRL-RV-PS-
TR-2022-0088

SMALL SATELLITE POSITION, NAVIGATION, AND TIMING INNOVATIONS VOLUME III - TWO WAY RANGING FOR TIME AND FREQUENCY TRANSFER IN LEO CONSTELLATIONS

Christopher Flood and Penina Axelrad

University of Colorado Boulder
Aerospace Engineering Sciences, CCAR
3775 Discovery Drive
Boulder, CO 80303

30 August 2022

Final Report

AIR FORCE RESEARCH LABORATORY
Space Vehicles Directorate
3550 Aberdeen Ave SE
AIR FORCE MATERIEL COMMAND
KIRTLAND AIR FORCE BASE, NM 87117-5776

DTIC COPY

NOTICE AND SIGNATURE PAGE

AFRL-RV-PS-TR-2022-0088 HAS BEEN REVIEWED AND IS APPROVED FOR PUBLICATION IN ACCORDANCE WITH ASSIGNED DISTRIBUTION STATEMENT.

//SIGNED//	//SIGNED//
_____	_____
Dr. Spencer E. Olson	Mark E. Roverse, Chief
Program Manager/AFRL/RVB	AFRL Geospace Technologies Division

REPORT DOCUMENTATION PAGE

Form Approved
OMB No. 0704-0188

1. REPORT DATE *(DD-MM-YYYY)*	**2. REPORT TYPE**	**3. DATES COVERED** *(From - To)*
30-08-2022	Final Report	4 Dec 2018 – 30 Aug 2022

4. TITLE AND SUBTITLE
Small Satellite Position, Navigation, and Timing Innovations
Vol. III – Two Way Ranging for Time and Frequency Transfer in LEO Constellations

5a. CONTRACT NUMBER
FA9453-19-1-0076

5b. GRANT NUMBER

5c. PROGRAM ELEMENT NUMBER
63401F

6. AUTHOR(S)
Christopher Flood and Penina Axelrad

5d. PROJECT NUMBER
3682

5e. TASK NUMBER
EF134353

5f. WORK UNIT NUMBER
V1NE

7. PERFORMING ORGANIZATION NAME(S) AND ADDRESS(ES)
University of Colorado Boulder
Aerospace Engineering Sciences, CCAR
3775 Discovery Drive
Boulder, CO 80303

8. PERFORMING ORGANIZATION REPORT NUMBER

9. SPONSORING / MONITORING AGENCY NAME(S) AND ADDRESS(ES)
Air Force Research Laboratory
Space Vehicles Directorate
3550 Aberdeen Avenue SE
Kirtland AFB, NM 87117-5776

10. SPONSOR/MONITOR'S ACRONYM(S)
AFRL/RVBYT

11. SPONSOR/MONITOR'S REPORT NUMBER(S)
AFRL-RV-PS-TR-2022-0088

12. DISTRIBUTION / AVAILABILITY STATEMENT
Approved for public release; distribution is unlimited (AFRL-2023-1731 dtd 12 Apr 2023).

13. SUPPLEMENTARY NOTES

14. ABSTRACT
This final report documents the work completed by researchers and students in the Colorado Center for Astrodynamics Research (CCAR) and Smead Aerospace Engineering Sciences at the University of Colorado Boulder, to model and develop technologies and algorithms to advance small space platform positioning, navigation, and timing, with a primary emphasis on timing systems. The report is presented in three volumes. Volume 1 presents the CONTACT software defined radio (SDR) based testbed for measurement and ensembling of low size, weight, and power (SWaP) atomic clocks. Volume 2 describes the development of a CSAC flight experiment to be flown on the MAXWELL UNP-9 CubeSat, expected to be launched in 2023. Volume 3 focuses on modeling and analysis of distributed optical time and frequency transfer across small satellites in a large-scale low Earth orbit (LEO) constellation.

15. SUBJECT TERMS
Optical time transfer, LEO constellaton

16. SECURITY CLASSIFICATION OF:			**17. LIMITATION OF ABSTRACT**	**18. NUMBER OF PAGES**	**19a. NAME OF RESPONSIBLE PERSON**
a. REPORT	**b. ABSTRACT**	**c. THIS PAGE**			**19b. TELEPHONE NUMBER** *(include area code)*
Unclassified	Unclassified	Unclassified	Unlimited	52	Dr. Spencer E Olson

This page is intentionally left blank.

TABLE OF CONTENTS

LIST OF FIGURES

Figure **Page**

LIST OF FIGURES (continued)

LIST OF TABLES

Acknowledgements

We acknowledge the valuable advice provided Dr. A. J. Metcalf, Dr. Benjamin Stuhl, and their colleagues at AFRL who attended our presentations and gave helpful feedback for moving forward with the project.

1 SUMMARY

This final report documents the work completed by researchers and students in the Colorado Center for Astrodynamics Research (CCAR) and Smead Aerospace Engineering Sciences at the University of Colorado Boulder, to model and develop technologies and algorithms to advance small space platform positioning, navigation, and timing, with a primary emphasis on timing systems. The report is presented in three volumes. Volume 1 presents a software defined radio (SDR) based testbed for measurement and ensembling of low size, weight, and power (SWaP) atomic clocks. Volume 2 describes the development of a CSAC flight experiment to be flown on the MAXWELL UNP-9 CubeSat, expected to be launched in 2023. Volume 3 focuses on modeling and analysis of distributed optical time and frequency transfer across small satellites in a large-scale low Earth orbit (LEO) constellation.

We present here an analysis of potential time and frequency transfer methods among satellites in a low Earth orbit (LEO) constellation, based on optical inter-satellite links (OISL) typically used for communication. The simulation considers an expanded functionality of the optical terminals to support dual one-way time transfer, with the goal of achieving clock synchronization across the constellation at the 5-100ps level. The capability for synchronization over an optical communications channel at this level was demonstrated for ground-based links [1]. This report provides an overview of proposed proliferated low Earth orbit (P-LEO) satellite constellations, range measurement models to simulate inter-satellite links, and estimation architectures to support clock estimation and orbit determination.

2 INTRODUCTION

In recent years, ground-based optical systems have been used for satellite ranging to support orbit determination [2], ground-to-space communication [3], and time transfer [4]. Conventional methods of satellite telemetry, tracking, and control (TTC) require one-to-one contact with specific ground stations, limiting satellite updates to periods when it is in view of a particular ground station. This model has historically worked well, with the onus of TTC spread across a number of independent spacecraft operators, and relatively small satellite constellation sizes (100). Over the past 5 years this paradigm has changed, as mega-constellations of small satellites (Starlink, Kuiper, OneWeb, Telesat) are currently being populated [5] to support worldwide broadband access, Earth observation, and various commercial and science goals. At the same time, research and development of space-qualified optical hardware has resulted in the deployment of large optical communication terminals [6] serving as the backbone of ESA's space data highway and other high data rate applications. Miniature versions of these optical terminals [7] have the capability to enable communication, ranging, and time transfer between small satellites in a constellation. The exponential growth in constellation size and the increase in technology readiness level of optical terminals present an opportunity for analysis of the impact of inter-satellite links on increased constellation autonomy.

Sections 3.1 - 3.2 below discuss commonly used time transfer and ranging systems along with their limitations. The satellite constellations, inter-satellite links, and inter-satellite range model are presented in Sections 3.5 - 3.7. The theory for using inter-satellite range measurements for clock state estimation and orbit determination is shown in Sections 3.8 and 3.9. We briefly discuss the impact of orbit errors and relativistic effects on time and frequency transfer in Sections 3.10 and 3.11.

Most theory is outlined in Section 3 with corresponding results in Section 4. All simulated clock profiles, inter-satellite range measurements, and estimation results are contained in Section 4. The report conclusions are presented in Section 5 followed by the references.

3 METHODS, ASSUMPTIONS, AND PROCEDURES

3.1 Existing Time Transfer Methods

Within the past 10 years a significant amount of progress has been made regarding optical atomic clocks [8]. A primary issue with most advanced clocks is that traditional time and frequency transfer methods are much noisier than the oscillators themselves - as such, these timescales that exist at national metrology institutes do not serve a purpose outside of the

laboratory environment.

There are many different ways to transfer time with varying degrees of accuracy. A few of these methods, along with the frequency regime and corresponding TDEV values at 100 seconds, are listed in Table 1. Methods such as GPS common view and Two-Way Satellite Time and Frequency Transfer (TWSTFT) are routinely used to compare extremely stable clocks at inter-continental baselines. Other methods, such as White Rabbit and Optical Two-Way Time and Frequency Transfer (TWTFT), have significant technical barriers to becoming global time transfer methods. A brief description of each time transfer method is provided in the sections below.

Table 1. Time Transfer Methods

Method	Frequency	TDEV, 100s
GPS One-Way [9]	RF	10 ns
GPS Common View [10]	RF	300 ps
LASSO [11]	Optical	<100 ps
GPS Carrier Phase [12],[13]	RF	<10 ps
TWSTFT [14]	RF	10 ps
Optical Comm [15]	Optical	10 ps
T2L2 [16]	Optical	2 ps
Optical Comm, PRBS [1]	Optical	1 ps
White Rabbit [17]	Optical	1 ps
Optical TWTFT [18]	Optical	1 fs

3.1.1 GPS One-Way

GPS receivers solve for the offset between the local clock and GPS Time when computing a position solution. The time transfer error from a satellite to receiver can be accomplished at the 10-15 ns level using coarse acquisition (C/A) codes [9]. This method is useful for clock synchronization across distributed devices, such as fault monitoring in electrical power systems [19], but is not used to compare highly stable clocks.

3.1.2 GPS Common View

In the GPS common view method two ground receivers simultaneously observe the same GPS satellite. Both ground stations compute their local clock offset with respect to GPS time and communicate results between stations. The measured values are subtracted, causing any common errors to drop out. The clock synchronization between two ground stations using GPS common view can be achieved at the nanosecond level [9] and can be averaged down to 300 picoseconds [10].

3.1.3 Laser Synchronization from Stationary Orbit (LASSO)

The LASSO system was a payload hosted on a GEO satellite in 1988 for clock comparison. The system operates at an optical frequency of 563.5 THz, and thus requires different hardware than RF methods at both the ground stations and the satellite. Satellite laser ranging (SLR) stations transmit laser pulses to the target satellite and measure the round trip time. Each ground station uses a highly stable clock, time tagging hardware, and detectors to precisely measure the departure and return times of the light pulses. The target satellite is equipped with retroreflectors that send the pulse back towards the transmitting ground station and detection / time tagging hardware to measure the pulse arrival time. Due to large distance to the satellite target, very few SLR stations were able to participate in LASSO clock comparison experiments [11].

The pulse departure time, arrival time at the satellite, and return time form a measurement referred to as a triplet. The offset between the satellite clock and the ground station clock is computed from these triplets. When two ground stations compare their clocks, they both lase the satellite, use the triplets to compute the satellite clock offset, and then exchange values to find the offset between ground station clocks. The uncertainty in the measurement is on the order of 100 picoseconds [11].

3.1.4 GPS Carrier Phase

Carrier phase GPS solutions use GPS signal phase as the observable as opposed to the C/A code. The benefit of using carrier phase measurements is that they can be up to 100 times more precise than code measurements [20]. One of the drawbacks is that carrier phase measurements provide ambiguous range, where the integer cycle ambiguity must be estimated to produce pseudorange measurements. Time transfer using GPS carrier phase solutions have been demonstrated at the 10 picosecond level [12], [13].

3.1.5 Two-Way Satellite Time and Frequency Transfer

Two-way satellite time and frequency transfer (TWSTFT) uses communication satellites in geostationary orbit (GEO) to compare clocks on the Earth separated by large distances. The carrier frequency is in the Ku band (10.7-14.5 GHz) with chipping rates of 1 MHz [21]. The maximum baseline for clock comparison is larger than in GPS common view as the common view satellite is up to 15,000 kilometers higher in altitude.

TWSTFT ground stations transmit ranging codes to the GEO satellite, which acts as a repeater, relaying the codes to the other ground station. A 1 pulse-per-second (PPS) signal is synthesized based on the transmitted signal at each station. A second 1 PPS signal is

generated from the received signal at each station; each of these PPS signals are used to start and stop a time interval counter (TIC) located at each ground station. The TIC output is a history of time intervals which is used to compute the offset between clocks [21]. Time transfer performance using this method has TDEV of 100 picoseconds at 1 second averaging intervals and 10 picoseconds for averaging intervals of 100 seconds [14].

3.1.6 Optical Communication

Communication between devices requires some level of synchronization to properly interpret transmitted information. The receiver clock may be stable over short intervals, but is almost guaranteed to drift out of synch if left uncorrected. Modern communication systems account for this by embedding timing information in the data stream for the receiving device to use in correcting its clock, a process known as clock recovery [22].

Clock recovery is an integral part of any communication system as accurate interpretation of modulated information depends on synchronized clocks. The synchronization requirements from the communications sector are not as strict as those in the navigation sector - most computer networks today use Network Time Protocol (NTP) for clock synchronization, which guarantees millisecond level synchronization. Methods developed at the Swedish National Laboratory in 2008 used an existing optical communication channel to transfer time at much higher precision than NTP. The design resulted in a time deviation of 30 picoseconds after 100 seconds of averaging [15].

The time transfer architecture was implemented on top of a 10-Gb/s fiber optic communication channel. Both outbound and inbound data streams are connected to custom built hardware that generates a pulse every time a certain data frame is identified. The pulses are used in a similar manner to TWSTFT where the pulse from the transmitted signal starts a time interval counter and the pulse from the received signal stops the TIC. The history of time intervals is used to compute the clock offset.

3.1.7 Time Transfer via Laser Link (T2L2)

Time transfer via laser link (T2L2) is a follow on to LASSO launched in 2008 as a payload on the Jason-2 satellite. The closer range of LEO satellites provides the opportunity for many more laser ranging stations to participate in time transfer experiments as compared to with LASSO. The principle of clock comparison is the same, with improvements in the space and ground segment hardware [23].

T2L2 requires ground laser stations and a satellite equipped with a retroreflector, time tagging equipment, and a stable on-board oscillator. A ground station transmits laser pulses to the satellite, recording the departure and return times. The satellite records the time of

pulse arrival. These three time values are used to compute the offset between the ground station and satellite clocks. A second ground station can simultaneously perform the same process. The clock offsets of each ground station with respect to the satellite are processed to produce the clock offset between ground stations. The time transfer stability between two ground stations was experimentally demonstrated to be a few picoseconds at 100 second averaging intervals [16].

3.1.8 Spread Spectrum Optical Communication

Experiments conducted by NIST [1] in 2018 demonstrated picosecond level time transfer using COTS free-space optical communication hardware. A communication link was established between co-located ground clocks with effectively 4 kilometers of separation. Each site modulates psuedorandom binary sequences (PRBS) on continuous wave laser light using binary phase-shift keyed (BPSK) modulation. The link operates in half-duplex configuration.

When data are transmitted from Site A to Site B, the time of signal departure and arrival is computed from the PRBS. After signal reception, Site B transmits a PRBS back to Site B and an additional pair of departure and arrival timestamps are created. These four values are used to compute the clock offset according to Equation 1, plus a calibration term ΔT_{cal}.

$$\Delta T_{AB} = \frac{T^A_{RX} - T^B_{TX}}{2} - \frac{T^B_{RX} - T^A_{TX}}{2} + \Delta T_{cal} \tag{1}$$

3.1.9 White Rabbit

White Rabbit is a network protocol using specialized hardware to achieve picosecond level synchronization between nodes. It was initially developed in 2008 at the European Organization for Nuclear Research (CERN) to synchronize the multitude of instruments and detectors involved in the Large Hadron Collider (LHC) [24]. White Rabbit has since evolved into a method used by national metrology institutes to compare clocks connected by fiber and separated by small baselines [17].

A White Rabbit architecture was implemented at NIST to evaluate the feasibility of using it to distribute UTC(NIST) across the campus. Loopback tests were conducted to evaluate the noise in the system and found time stability below 20 picoseconds at all averaging intervals [17].

3.1.10 Optical TWTFT

Recent work by NIST in 2016 has enabled comparison of optical time scales at the femtosecond level [18]. Optical time scales produce optical frequencies, which are translated to RF using a frequency comb locked to the the cavity-stabilized laser. The frequency comb outputs a pulse train at radio frequencies and is used as a traditional oscillator with the stability benefits of the underlying optical time scale.

In this experiment two time scales transmit optical pulses across a 4 kilometer free-space link. An initial coarse time transfer, based on methods in Section 3.1.8, is used to calibrate the link prior to achieving sub-femtosecond results. The pulse departure and arrival times in the respective time scales, as determined by Linear Optical Sampling (LOS) techniques [18], are used to compute the relative time offset. An optical communication channel is used for real time feedback between sites to synchronize the two time scales.

The NIST system demonstrates state-of-the-art time transfer between two optical time scales. Laboratory grade, high SWaP-C hardware is required to achieve this level of precision, restricting this method primarily to ground experiments for now. Current research is underway with respect to lower SWaP-C flight experiments with optical oscillators and frequency combs.

3.2 Existing Inter-satellite Ranging

Inter-satellite ranging between small satellites on orbit does not currently occur at large scales; with the proposed constellations in Section 3.5 that may soon change. One-way ranging from GPS in support of navigation is currently the most common type of one-way, satellite-to-satellite ranging. In the sections below we discuss two satellite missions that use RF ranging and optical inter-satellite interferometry in support of measuring variations in Earth and Lunar gravity fields.

3.2.1 GRACE & GRACE-FO

The Gravity Recovery and Climate Experiment (GRACE) [25] launched in 2002 and operated until end of life in 2017. GRACE consisted of two identical satellites that acted as a single instrument designed to measure variations in Earth's gravity field. The satellites were placed on the same orbit approximately 200 kilometers apart and measured the changes in inter-satellite range using a K-band ranging system. The measured fluctuations in range are used to compute monthly estimates of Earth's gravity field. The K/Ka band ranging (KBR) system on GRACE makes carrier phase measurements to determine variations in inter-satellite separation. Two frequencies are used to remove the frequency-dependent

ionospheric effects on signal propagation. The precision of the KBR system is better than 10μm.

The GRACE-FO mission was designed to be functionally identical to GRACE and shares much of the same design heritage. One of the key technological additions is a laser ranging interferometer (LRI) which measures inter-satellite range to a much higher precision as a result of fewer uncertainties and much smaller wavelength at optical frequencies. One satellite acts as the frequency reference to which the other satellite will phase lock. In Figure 1 the left satellite is the optical frequency reference and the right satellite will phase lock its laser to this incoming beam. The secondary satellite transmits a beam back to the primary satellite with a fixed 10 MHz offset. Each satellite mixes the incoming signal against its local oscillator, generating a 10 MHz beat note. Relative motion between the two satellites will change the exact frequency of the beat note, which contains information regarding the gravity signal of interest. This interferometric method of measurement is fundamentally different than the KBR system and yields an improved noise figure of 0.3 nm / $\sqrt{\text{Hz}}$ [26].

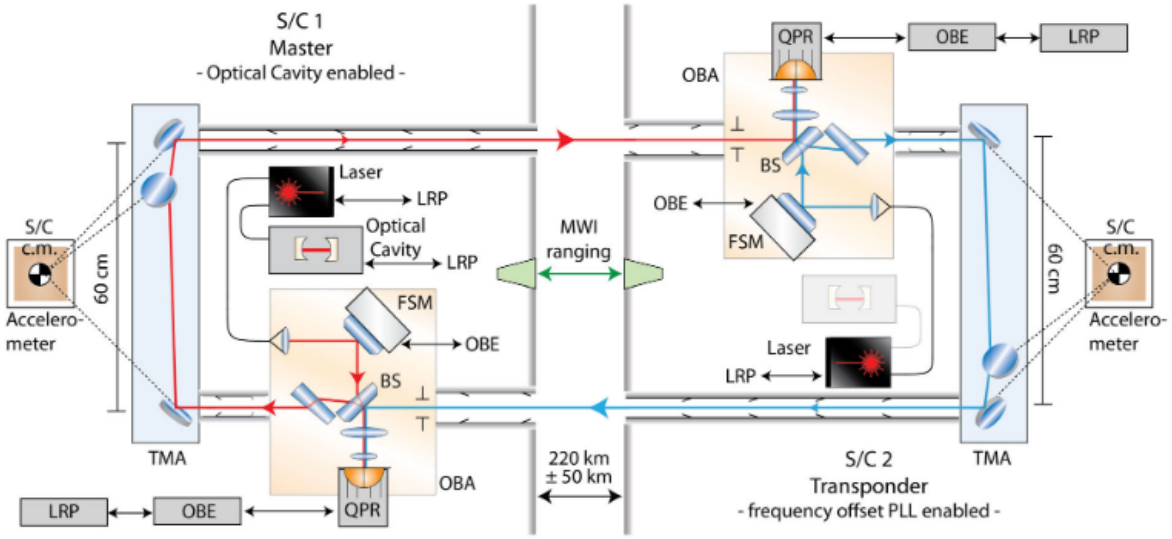

Figure 1. GRACE-FO LRI from [26], FIG. 1

3.2.2 GRAIL

GRACE was such a success that it inspired a similar mission mapping the Moon's gravity field, the Gravity Recovery and Interior Laboratory (GRAIL) [27]. The inter-satellite ranging system on GRAIL is the lunar gravity ranging system (LGRS) [28]. The mission architecture is quite similar to GRACE in that two satellites act as a single instrument to measure variations in the gravity field. The LGRS makes carrier phase range measurements at Ka band and performs two-way time transfer in S band. The demonstrated sensitivity of the

inter-satellite range measurement is 0.6 μm / $\sqrt{\text{Hz}}$.

Figure 2 below shows the types of signals going between satellites and from the satellites back to Earth. Figure 3 is a more detailed view of the measurement system onboard each spacecraft.

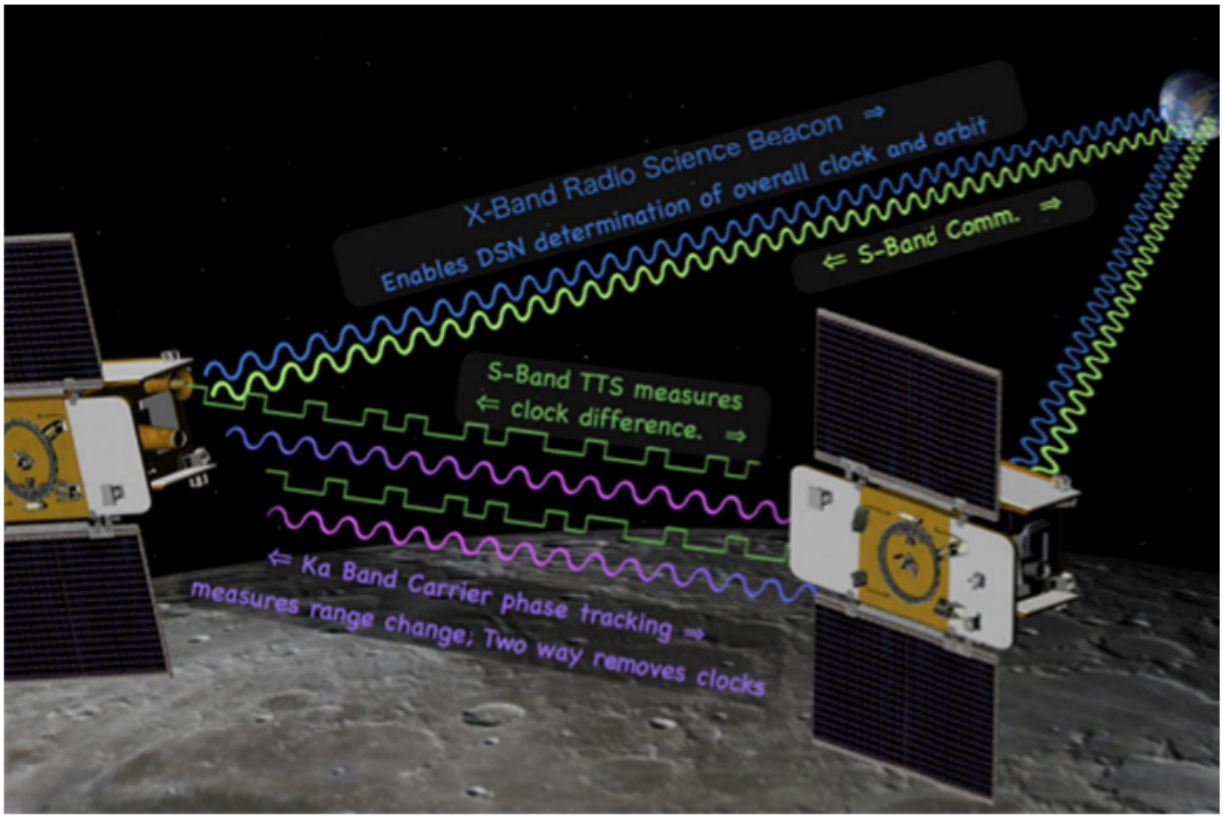

Figure 2. GRAIL Satellites from [28], Fig. 1

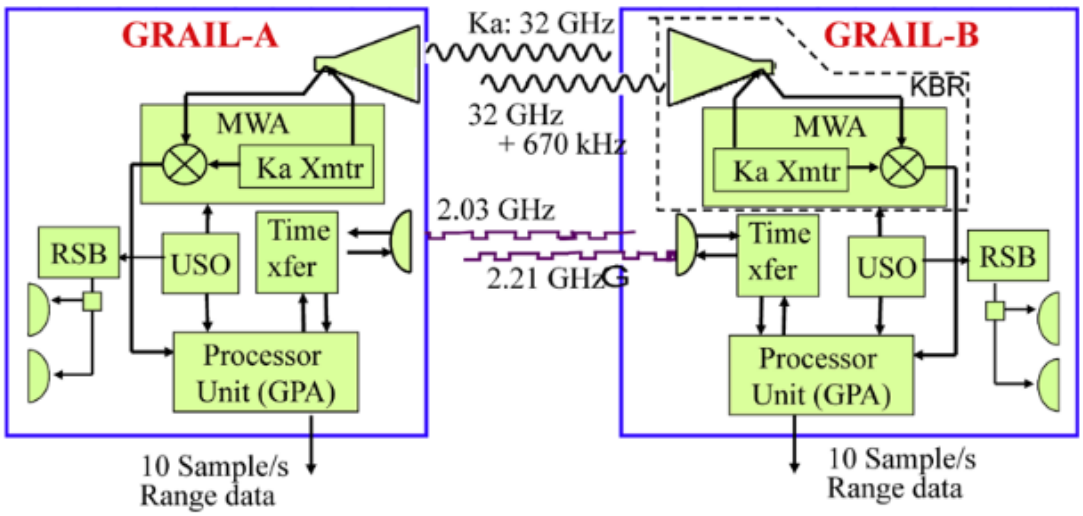

Figure 3. GRAIL Measurement System from [28], Fig. 2

3.3 Clock Profiles

In this research we are modeling atomic clocks onboard spacecraft in a satellite constellation. The clock profiles are given by the phase and frequency time series for all simulated oscillators. We use a simple two state dynamic clock model, with the process noise covariance matrix based on oscillator specific stability parameters. The discrete time model used in the project is shown in the equations below [29].

$$x_{k+1} = \phi(\tau)x_k + w_k \,, \tag{2}$$

where the state transition matrix is defined by:

$$\phi(\tau) = \begin{bmatrix} 1 & \tau \\ 0 & 1 \end{bmatrix}, \tag{3}$$

and process noise vector with covariance:

$$w_k \sim \mathcal{N}(0, Q(\tau)) \tag{4}$$

$$Q(\tau) = \begin{bmatrix} q_1\tau + \frac{q_2\tau^3}{3} & \frac{q_2\tau^2}{2} \\ \frac{q_2\tau^2}{2} & q_2\tau \end{bmatrix} \tag{5}$$

The process noise is assumed to be Gaussian and zero mean with covariance $Q(\tau)$ described

by white and random walk frequency noise parameters, q_1 and q_2. These noise parameters are specific to each clock. Realizations of this noise are represented by the noise vector - Equation 4 - and are incorporated into the propagation according to Equation 2. Simulated phase and frequency data representing clocks in a satellite constellation are shown in Section 4.1.

3.4 Clock Stability

A variety of statistical quantities are used to describe underlying noise properties that determine frequency stability for an oscillator. Each of these tools can reveal different types of underlying noise processes in the clock that appear at different averaging intervals. In this work we use overlapping Allan deviation (OADEV) for quantifying frequency stability and time deviation (TDEV) to quantify how long a timing requirement can be met. The subsections below are based on a significant amount of information from Riley's *Handbook of Frequency Analysis* [30].

3.4.1 Allan Variance

The Allan variance is the most common value used to represent frequency stability. It was introduced by David Allan in 1966 as a method to distinguish flicker frequency noise from white noise [31]. The original two-sample Allan variance can be computed from phase data using Equation 6. The square root of the variance, the Allan deviation, is usually used instead of the variance. The uncertainty of a computed ADEV value is often approximated as $\pm\sigma_y(\tau)/\sqrt{N}$.

$$\sigma_y^2(\tau) = \frac{1}{2(N-2)\tau^2} \sum_{i=1}^{N-2} [x_{i+2} - 2x_{i+1} + x_i]^2 \tag{6}$$

3.4.2 Overlapping Allan Variance

The overlapping Allan variance is based on the Allan variance, but uses overlapping samples to reduce the uncertainty in computed variance values. Overlapping the samples to reduce the variance comes at the cost of additional computing time. A comparison of the traditional Allan variance and overlapping Allan variance is shown in Figure 4.

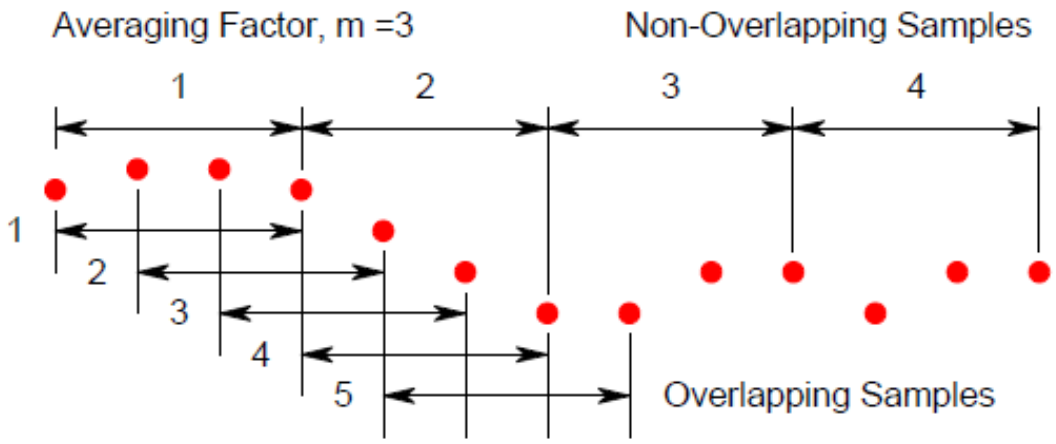

Figure 4. Comparison of Non-Overlapping and Overlapping Allan Deviation [30]

The formula for computing overlapping Allan variance is shown in Equation 7. It has the same general form as Equation 6 with the addition of an averaging factor, m. The averaging factor is defined as $m = \frac{\tau}{\tau_0}$ with τ_0 the time interval between two adjacent phase measurements.

$$\sigma_y^2(\tau) = \frac{1}{2(N-2m)\tau^2} \sum_{i=1}^{N-2m} [x_{i+2m} - 2x_{i+m} + x_i]^2 \tag{7}$$

3.4.3 Modified Allan Variance

The modified Allan variance uses additional averaging to distinguish between white and flicker noise, as these two noise processes are indistinguishable in an overlapping Allan variance plot. The formula for computing modified Allan variance is given in Equation 8.

$$Mod\,\sigma_y^2(\tau) = \frac{1}{2m^2\tau^2(N-3m)+1} \sum_{j=1}^{N-3m+1} \left[\sum_{i=j}^{j+m-1} x_{i+2m} - 2x_{i+m} + x_i \right]^2 \tag{8}$$

3.4.4 Time Variance

Time variance represents the time stability of an oscillator and is computed from the modified Allan variance. The time deviation can be used to predict how long a clock deviation stays below a time error threshold based on the underlying frequency stability. This time domain metric can be used to determine the required update rate of a system and better inform design decisions regarding the clock stability required for a mission.

$$\sigma_x^2(\tau) = \frac{\tau^2}{3} Mod\, \sigma_y^2(\tau) \tag{9}$$

The time deviation for five atomic oscillators is shown in Figure 5. A reasonably easy clock synchronization requirement is one nanosecond. After an ideal clock update, the frequency stability of a Microsemi CSAC predicts that time uncertainty under one nanosecond can be maintained for 100 seconds. Much larger and more expensive clocks can keep the time uncertainty within a nanosecond for all time intervals shown on the graph. A much more challenging time uncertainty threshold is one picosecond. Following an ideal clock synchronization, the frequency instability in the CSAC is so large that it cannot maintain a picosecond time uncertainty for any averaging interval listed here. The RAFS oscillator can maintain it for a few seconds, ORAFS and ACES for 100 seconds, and the hydroden maser for 1000 seconds.

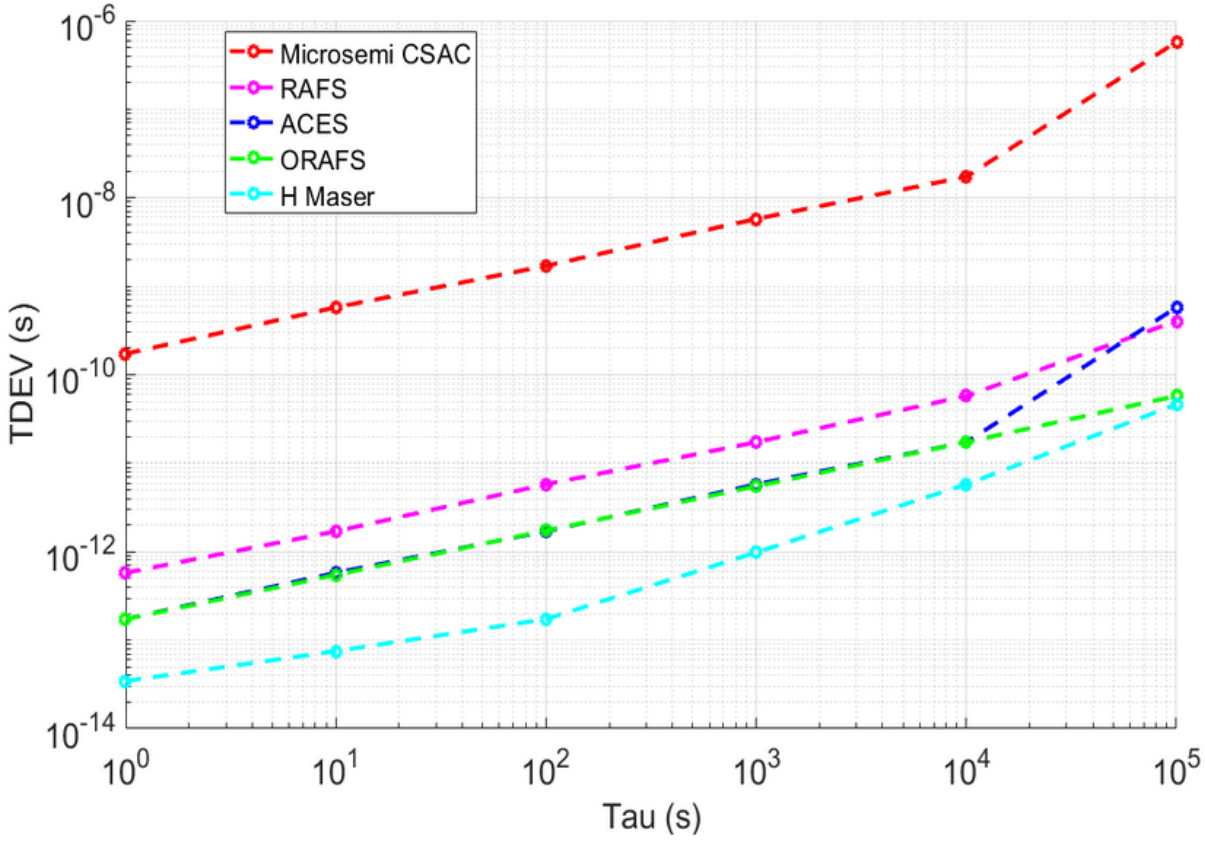

Figure 5. TDEV of Clocks

The time deviation equation can be used to solve for when the averaging interval, τ, results in a specified time error. Four time error requirements are listed in Table 2 along with the averaging intervals corresponding to that time error for the five clocks. Information from this table can be used to design a minimum system update rate to resynchronize the oscillator

in order to keep time error below a desired threshold.

Table 2. Clock Update Interval Based on Time Error Requirement

Clock / Time Requirement	1ps	10ps	100ps	1ns
CSAC	N/A	N/A	1s	30s
RAFS	3s	400s	20,000s	>100,000s
DARPA ACES	30s	4,000s	30,000s	>100,000s
ORAFS	30s	4,000s	>100,000s	>100,000s
H-Maser	1,000s	20,000s	>100,000s	>100,000s

3.5 Satellite Constellations

Over the past 10 years the satellite design paradigm has largely shifted from building expensive, highly redundant, state-of-the-art single satellites to building large numbers of lower cost, moderately capable, small satellites with room for some level of attrition [5]. One of the significant factors behind this push is the increased frequency and decreased cost to put objects in orbit, primarily due reuseable launch vehicle capabilities developed by SpaceX. An additional benefit is a more agile approach to satellite design and deployment which can take advantage of new technologies that become available from launch to launch.

The plans for next generation mega-constellations contain tens of thousands of satellites in their final versions. The primary motivation from the private sector is to provide a global broadband service without the monumental cost of installing cable infrastructure across continents. In contrast to the private sector, the scale of proposed constellations from the public sector is much smaller with priorities focused on advanced communication for military users; navigation systems to augment or replace GPS in GNSS denied environments, and Earth observation goals.

The two proposed constellations studied in our project are DARPA Blackjack [32] and SDA Transport Layer [33]. A single GEO satellite is modeled along with each LEO constellation. The position, velocity, and clock states of the GEO spacecraft are treated as perfectly known, replacing the traditional role of ground station support.

These constellations are designed using NASA's open source mission design software [34], the General Mission Analysis Tool (GMAT). GMAT enables the use of high-fidelity orbit dynamics, such as Earth's gravity field and point mass influence from third bodies, as well as suite of propagation methods to choose from. GMAT can be used through the graphical user interface (GUI) or the application programming interface (API) for integration into languages such as MATLAB, Python, or Java - this project uses the GMAT API in MATLAB.

3.5.1 DARPA Blackjack Pit Boss

The Blackjack Pit Boss program is designed to create a P-LEO system that delivers relevant data to subscribers in a timely manner, without direction from ground operators or data processing on the ground. Initial versions of the constellation consists of two circular, polar orbit planes with 10 satellites in each at 1,000 kilometers in altitude [32]. The representation of this constellation used for our studies is presented in Section 4.2.2. The constellation has orbit planes separated by 10° in right ascension with satellites in adjacent planes offset by 18° with respect to the primary plane.

3.5.2 SDA Transport Layer

The Space Development Agency (SDA) is constructing a Transport Layer in LEO comprised as a constellation of 300-500 satellites at altitudes of 750-1200 kilometers. The Transport Layer and Blackjack Pit Boss have similar technological goals with the long term vision of the Transport Layer being an operational system. Satellites within the constellation will communicate via optical inter-satellite links (OISL) and use RF for ground support. The constellation design ensures that 99% of locations on the Earth will have at least one satellite in view at all times. The constellation configuration used for our studies is shown in Section 4.2.1; it has 18 orbit planes separated by 10° in right ascension with 10 satellites in each plane. Satellites in adjacent planes are offset by 2 ° in argument of latitude with respect to the previous plane.

3.6 Optical Inter-Satellite Links

Optical links for small satellites are an emerging technology for inter-satellite communication. Both the Blackjack Pit Boss, Transport Layer, and other space missions are looking to incorporate optical terminals into spacecraft design due to potential for improved data rates, lower loss, higher signal-to-noise ratio, and communication channel security. Various companies are currently developing low SWaP optical terminals for use on small satellites [7].

In the satellite simulations, optical inter-satellite links are modeled along the three primary spacecraft axes, enabling full constellation inter-connectivity. In order to effectively range or communicate using OISLs, the linked satellites need to be able to direct energy from a transmitting laser terminal to a target laser terminal. The locations of the sensors on the spacecraft and the sensor field of view will limit the portions of the trajectory when sensors can reliably communicate with each other. In our study we assume all spacecraft are nadir pointing throughout their orbits, neglecting any complications of attitude control for now.

The off-boresight field of view, shown by θ in Figure 6, for each terminal is limited to a 20°cone for a link to be established.

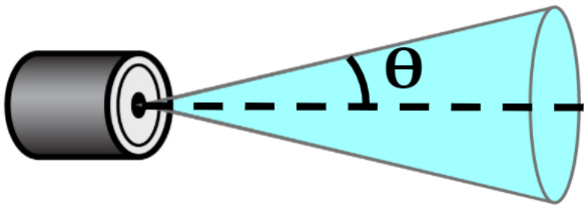

Figure 6. Optical Sensor Field of View

3.7 Two-Way Inter-satellite Range Model

Small satellites that use GPS for navigation rely on one-way radiometric measurements. The error in one-way ranging systems have a $\frac{1}{c}$ correlation with clock error at both the receiver and the transmitter. Using range to solve for receiver location or clock offset is therefore related to knowledge of transmitter location and clock error contributions. In a two-way system, the path reciprocity significantly reduces the errors from uncertainty in knowledge of location and clock effects. With stationary participants in an inertial frame, the signal path is completely reciprocal. In the case of relative motion with respect to the inertial frame, as is the case with inter-satellite links, the signal path is only partially reciprocal. This reduces the correlation between clock and position knowledge from $\frac{1}{c}$ to order $\frac{1}{c^2}$ and higher.

3.7.1 Dual One Way

In this work we model inter-satellite range as a set of dual one-way measurements as discussed in Section 3.2. One difference here is that instead of making carrier phase or interferometric measurements, pseudorandom binary sequences are assumed to generate an unambiguous range measurement between satellites. The range between satellites A and B is modeled using Equation 10. The components of the model include the coordinate time of signal transmission and reception, the clock offset of each satellite, and measurement noise.

The signal time-of-flight is represented by the difference between the coordinate time of transmission and reception. This is generated in simulation by accounting for receiver platform motion during the signal time-of-flight. The effects of transmitter and receiver clock errors are included on the range measurement, represented by $b_B(T_{RX})$ as the clock offset of the receiver at the time of signal reception and $b_A(T_{TX})$ as the clock offset of the transmitter at the time of signal transmission.

$$\rho_{AB} = c \cdot (T_{RX} - T_{TX} + b_B(T_{RX}) - b_A(T_{TX})) + \sigma_{noise} \tag{10}$$

The magnitude of the measurement noise in Equation 10 has a significant impact on the ability to estimate the clock states and transfer time. A small measurement noise will result in a better clock estimate, but may not be a realistic representation of noise figures in existing optical systems. Current literature [35] suggests that optical measurement noise is 30 – 100ps. The lower value is from the Atomic Clock Ensemble in Space (ACES) optical time transfer system [36] and the upper end of the range is based on reported values of the Time Transfer by Laser Link (T2L2) system [37]. This information is used to establish realistic bounds on the levels of measurement noise that should be considered.

Examples of range between satellites are presented in Section 4.3.

3.8 Clock State Estimation

Time transfer between satellite platforms is performed via estimation techniques using inter-satellite ranging measurements. The time error of both clocks, frequency error of the transmitting clock, and measurement noise all impact the range measurement. A conventional Kalman filter estimates the clock states for all satellites using the range observable as well as models for dynamics and measurements.

3.8.1 Clock Model

The clock states and state transition matrix for two satellites, A and B, are shown below. The full system model incorporates 180 clocks resulting in a global state vector with 360 total elements. The full state transition matrix is square with dimension 360 and block diagonal with $\phi(\tau)$ along the diagonal. A subset of the full constellation state is shown here for compactness.

$$x_{AB} = \begin{bmatrix} b_A \\ f_A \\ b_B \\ f_B \end{bmatrix}, \qquad \phi_k(\tau) = \begin{bmatrix} 1 & \tau & 0 & 0 \\ 0 & 1 & 0 & 0 \\ 0 & 0 & 1 & \tau \\ 0 & 0 & 0 & 1 \end{bmatrix} \tag{11}$$

3.8.2 Measurement Model

The inputs to the system are inter-satellite range measurements between satellites in the constellation.

The range model for a pair of inter-satellite range measurements is shown below in Equation 12 and 13.

$$\rho_{AB} = c \cdot \tau_{AB} + b_B(T_{RX}) - b_A(T_{RX}) + \tau_{AB} f_A + \sigma_{noise} \tag{12}$$

$$\rho_{BA} = c \cdot \tau_{BA} + b_A(T_{RX}) - b_B(T_{RX}) + \tau_{BA} f_B + \sigma_{noise} \tag{13}$$

For this analysis we consider the signal time of flight, τ, to be perfectly known. When this is the case, there is a linear relationship between the measurement and estimated state. The measurement sensitivity matrix, H, is written below in Equation 15.

$$z_{AB} = H x_{AB} + v_{AB} \tag{14}$$

$$H = \begin{bmatrix} -1 & \tau_{AB} & 1 & 0 \\ 1 & 0 & -1 & \tau_{BA} \end{bmatrix} \tag{15}$$

3.8.3 Estimation Implementation

The truth position and velocity ephemerides were generated by propagating each satellite state with GMAT at a 1 second time step. The clock signatures were created in parallel using a two-state clock model and process noise generated from the noise statistics of the RAFS clock. Inter-satellite range measurements were also generated at 1 second measurement intervals between valid satellite combinations. The measurements are processed in a conventional Kalman Filter to estimate the offset and frequency of the clocks in the satellite constellation.

Centralized Estimation The standard application of a CKF to this problem is to have one state estimate of all the clocks, a single state prediction step, and a single measurement update which uses all the measurements at once. This is easy to do in simulation and yields good estimation results, but implies the following operational requirements: 1) transmission of all measurements to a central location, 2) back propagation of the measurement updated state to each member of the constellation, and 3) a processing latency of the filter that is faster than the measurement rate. As constellations grow in size, this centralized approach does not scale well.

Decentralized Estimation An alternative is a decentralized estimation approach which fuses data using covariance intersection methods [38]. In this architecture each member of the constellation maintains a local copy of the entire constellation state and the time update

remains the same as in the centralized case. The local measurement update consists of three steps: 1) perform the measurement update with range measurements made locally, 2) broadcast your measurement updated state to all directly linked satellites, 3) fuse your pre-measurement updated covariance and state with the post-measurement updated covariance and states received from neighboring satellites, and 4) use the measurements made locally for a final measurement update with the fused state estimate. This process ensures that information is not reused and that correlations between state estimates in the constellation are correctly captured. Equation 16 shows the process for fusing two covariance matrices by adding the information matrices, P_{XX}^{-1} scaled by individual weights, ω. Once the fused covariance is computed, Equation 17 can be used to solve for the fused state variable, c. We extend these equations to N estimates and use equal weights for the clock state fusion.

$$\mathbf{P}_{cc}^{-1} = \omega \mathbf{P}_{aa}^{-1} + (1-\omega)\mathbf{P}_{bb}^{-1} \tag{16}$$

$$\mathbf{P}_{cc}^{-1}\mathbf{c} = \omega \mathbf{P}_{aa}^{-1}\mathbf{a} + (1-\omega)\mathbf{P}_{bb}^{-1}\mathbf{b} \tag{17}$$

3.9 Orbit Determination and Clock State Estimation

The orbital states of the satellites can be estimated using the range measurements in an Extended Kalman Filter (EKF). A single, centralized filter is used which assumes that all measurements are transmitted to a central location and a global estimate for all satellite states is produced. The communication channels required for this data relay are not currently modelled and we assume that the latency in communication is smaller than the EKF update frequency.

3.9.1 Dynamics Model

The state vector for a single satellite is shown below along with the nonlinear dynamics. The inclusion of the position and velocity components in addition to clock states results in a total of 8 states per simulated spacecraft. The equations of motion are used to propagate the position and velocity of each spacecraft forward in time.

NASA's General Mission Analysis Tool [34] software is used for high fidelity modeling of spacecraft dynamics, including Earth's gravity field, third-body influences, and non-gravitational forces. The clock state propagation remains linear and is handled independently of spacecraft position and velocity.

$$\mathbf{x}_A = \begin{bmatrix} x_A \\ y_A \\ z_A \\ \dot{x}_A \\ \dot{y}_A \\ \dot{z}_A \\ b_A \\ f_A \end{bmatrix}, \qquad \dot{\mathbf{x}}_A = \begin{bmatrix} f_x(\mathbf{x},t) \\ f_y(\mathbf{x},t) \\ f_z(\mathbf{x},t) \\ f_{\dot{x}}(\mathbf{x},t) \\ f_{\dot{y}}(\mathbf{x},t) \\ f_{\dot{z}}(\mathbf{x},t) \\ f_b(\mathbf{x},t) \\ f_f(\mathbf{x},t) \end{bmatrix} \tag{18}$$

3.9.2 Measurement Model

The inclusion of the satellite state as estimated parameters results in a non-linear measurement sensitivity matrix. Equation 19 shows the general form of the inter-satellite range measurement remains the same, however we are now estimating variables comprised within the geometric range, shown in Equation 20. The partial derivative of the measurement with respect to the state is then used to generate H.

$$\rho_{AB} = R_{AB} + b_B(T_{RX}) - b_A(T_{RX}) + \tau_{AB} f_A + \sigma_{noise} \tag{19}$$

$$R_{AB} = \sqrt{(x_B(T_{RX}) - x_A(T_{TX}))^2 + (y_B(T_{RX}) - y_A(T_{TX}))^2 + (z_B(T_{RX}) - z_A(T_{TX}))^2} \tag{20}$$

$$H = \begin{bmatrix} \frac{\partial \rho_{AB}}{\partial x_A} & \cdots & \frac{\partial \rho_{AB}}{\partial f_A} & \frac{\partial \rho_{AB}}{\partial x_B} & \cdots & \frac{\partial \rho_{AB}}{\partial f_B} \end{bmatrix} \tag{21}$$

3.9.3 Estimation Implementation

The truth position and velocity ephemerides were generated by propagating each satellite state with GMAT at a 10 second time step. The clock signatures were created in parallel using a two-state clock model and process noise generated from the noise statistics of the RAFS clock. Inter-satellite range measurements were also generated at 10 second measurement intervals between valid satellite combinations. The measurements are processed in a Extended Kalman filter to estimate the position, velocity, and clock states in the satellite constellation.

3.10 Effect of Orbit Errors on Time Transfer

Errors in orbit knowledge will affect time transfer accuracy - this is perhaps most easily demonstrated in GPS time transfer between a single satellite and a ground station with perfect knowledge of position. The modeled geometric range between the satellite at the

time of transmission and ground station at the time of reception is based on orbit parameters broadcast by the GPS satellite. Computing the satellite position based on the orbit parameters will not result in a perfect solution - any errors in the computed position along the range direction will manifest in the computed clock offset to the order $\frac{1}{c}$. Time transfer with picosecond accuracy thus implies orbit knowledge on the order of $\approx 300\mu$m - a stringent requirement that few satellites, if any, meet.

All one-way ranging and time transfer systems suffer from the same $\frac{1}{c}$ dependence on positional knowledge. In two-way systems, path reciprocity reduces the impact of state error from $\frac{1}{c}$ to $\frac{1}{c^2}$ and higher order. A relativistic derivation of time and frequency transfer in the context of the Atomic Clock Ensemble in Space (ACES) [39] computes orbit error limits for ISS to achieve the mission goals. The mission plan is to fly two atomic clocks on the ISS with frequency stability in the range of 10^{-16}. In order to compare the space clock performance with clocks on the ground a time transfer system similar to T2L2 will be placed on station. The analysis determined that ISS orbit errors of 10 meters would still satisfy the ACES frequency comparison requirement - being able to compare clocks at the 10^{-16} level after 10 days of averaging.

Another group [40] performed a similar relativistic analysis for a theoretical navigation constellation in MEO. The models for potential and velocity induced effects on oscillator frequency are similar, but the approach for studying the influence of orbit errors on frequency transfer is slightly different. The orbit error impact on second order Doppler and potential are treated separately, resulting in stricter error requirements than previously discussed. We assume the results discussed in the two aforementioned papers define lower and upper bounds on the range of tolerable orbit errors for clock comparison.

3.11 Relativistic Effects on Time & Frequency Transfer

The special and general theories of relativity describes how oscillator frequency is observer dependent. Two commonly modelled components are the impact of relative motion and differences in gravitational potential on apparent frequency. The relationship between proper time and coordinate time was derived in [39] and is shown below.

$$\frac{d\tau}{dt} = 1 - \left(\frac{U(t, \mathbf{x})}{c^2} + \frac{v^2(t)}{2c^2} \right) + O(c^{-4}) \tag{22}$$

The frequency stability of many existing commercial clocks is better than relativity induced perturbations, implying that any time and frequency transfer framework must be approached in a relativistic sense. The sections below discuss the velocity and potential based effects that impact proper time as measured on satellite clocks.

3.11.1 Relative Velocity

The classic thought experiment from Albert Einstein demonstrating the observer dependence implied by special relativity involves a light source at the center of a train car moving with constant velocity [41]. As soon as the light is turned on, a passenger on the train will observe the light hitting the far end of the train car walls at the same instant. From the perspective of an observer watching the train pass, the light will hit the rear end of the train before hitting the front of the train. Both observations are valid, yet yield different results.

The apparent paradox presented above is extensible to a moving oscillator, demonstrating the effects of relative motion on observed frequency. Imagine an oscillator that consists of a light pulse bouncing back and forth between two mirrors, as shown in Figure 7. Assuming that L does not change, the mirrors are perfectly reflective, and the constancy of the speed of light, the light pulsing back and forth can be used as a clock with period given by Equation 23. Now assume that a second identical clock is moving relative to the first clock with constant velocity, v, as shown in Figure 8. With relative motion between the two clocks, the light path appears to travel a longer distance between mirror reflections. Since the speed of light is constant in all reference frames [42], the period of this clock is larger than the period of the stationary clock and is given by Equation 24. Over time, the moving clock will lose time when compared to the stationary clock.

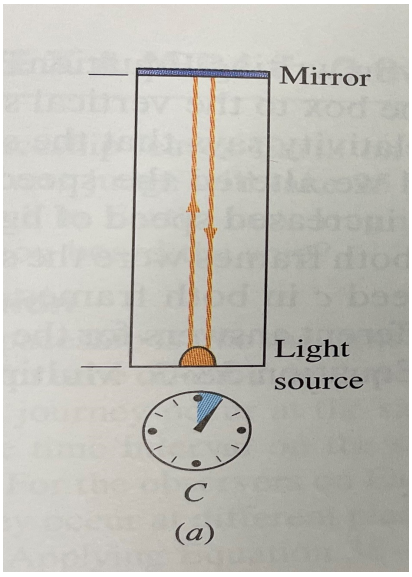

Figure 7. Stationary Clock from [43]

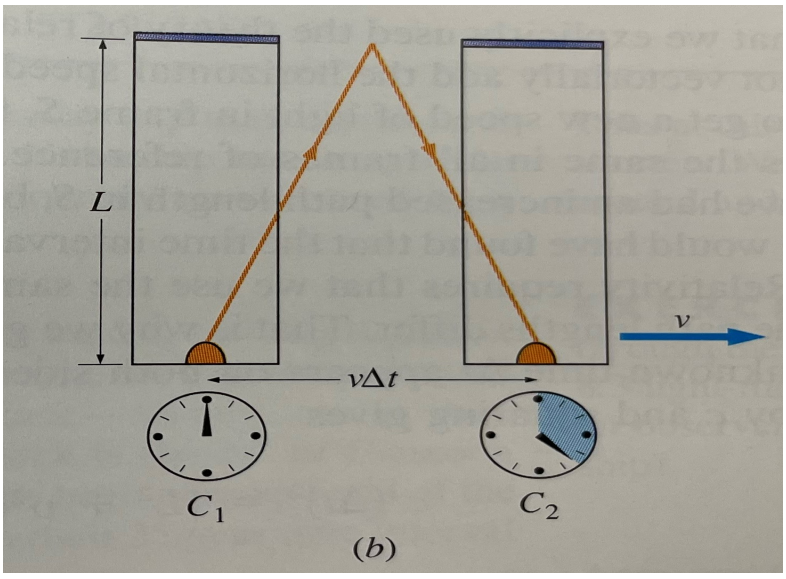

Figure 8. Clock in Relative Motion from [43]

$$\Delta t = \frac{2L}{c} \tag{23}$$

$$\Delta t' = \frac{\Delta t}{\sqrt{1 - \frac{v^2}{c^2}}} \tag{24}$$

The effect of relative velocity on the observed frequency of oscillators is particularly important to account for with oscillators on-board satellites. With stable atomic clocks, the velocity of satellites in orbit, and the desired levels of clock synchronization accuracy, the time dilation cannot be ignored. The effect of relative velocity on observed frequency is shown in Section 4.6.1.

3.11.2 Gravitational Potential

Differences in gravitational potential also impact elapsed time measurements for observers at separate locations. The principles were derived in 1907 [44] as an outcome of accelerated frames in the framework of special relativity and the Einstein equivalence principle. According to the theory, clocks farther from gravitational sources will tick faster than a clock closer to the gravitational source. There are two sources of potential that affect spacecraft in orbit: the non-uniform gravitational field of the Earth and the third body potential from the Moon, Sun, and other planets.

Earth's Geopotential The gravity field of the Earth is quite non-uniform, due to the rotation and uneven mass distribution. The rotation of the Earth about its spin axis causes a flattening which results in a larger radius at the equator than at the north pole by approximately 21 kilometers. Satellite missions specifically designed to map Earth's gravity field have resulted in high resolution maps of Earth's mass. The most detailed measurements of Earth's gravity field to date were provided by satellite missions such as GRACE [45], GOCE [46], and GRACE-FO [47].

Earth's gravity field is most commonly represented by spherical harmonics and a set of coefficients that scale each contribution. Equation 25 shows the calculation used to represent gravitational potential as a function of latitude, longitude, and radius. $\bar{P}_{nm}$ are Legendre polynomials and $\bar{C}_{nm}$, $\bar{S}_{nm}$ are time dependent coefficients provided by NASA. The trajectory of a spacecraft must be represented in an Earth fixed frame to compute geopotential contributions.

The size of the frequency shift is used to determine the model precision required. Using a trajectory generated with the highest model fidelity, the maximum absolute contribution of each degree can be computed and evaluated. If the maximum frequency shift is smaller than the frequency accuracy of the oscillator onboard the spacecraft, all degrees larger need not be modeled. Results from this analysis are presented in Section 4.6.2.

$$V_E = \frac{GM}{r}\sum_{n=0}^{\infty}(\frac{r_E}{r})^n \sum_{m=0}^{n} \bar{P}_{nm}(\sin\phi)[\bar{C}_{nm}\cos m\lambda + \bar{S}_{nm}\cos m\lambda] \tag{25}$$

Celestial Bodies All celestial bodies will contribute to the potential field of the spacecraft, affecting both the trajectory and observed frequency of the onboard oscillator. A diagram showing the geometry between the Earth (E), spacecraft (S), and celestial body (C) is presented in Figure 9. For most Earth orbiting spacecraft the largest contributions come from the Sun, due to its mass, and the Moon as a result of its proximity to the Earth. Third body effects of inner and outer planets are often not modeled due to their small contributions to the trajectory.

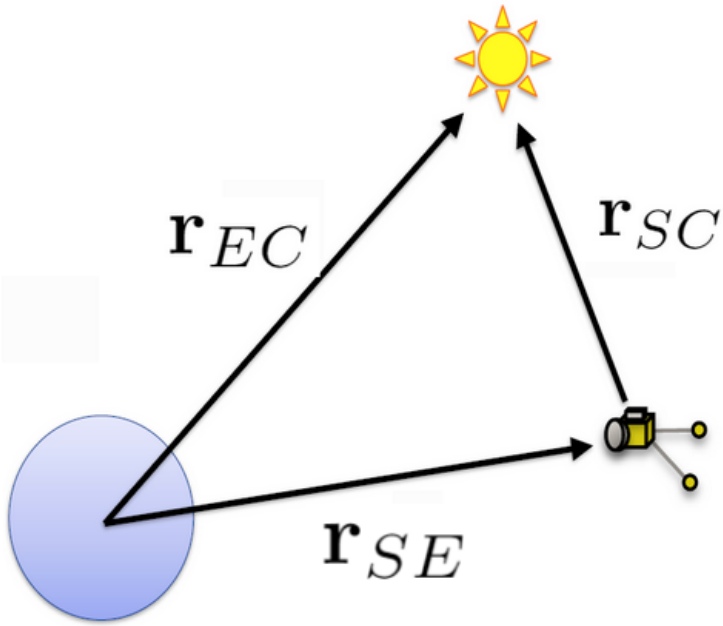

Figure 9. Third Body Diagram

The effect of planets on the potential experienced by the satellite will vary over time due to relative motion between Earth's orbit and the planet's orbit. This results in high and low frequency oscillations in the computed potential. Equation 26 is used to compute the potential contribution from third bodies. Results from this computation are shown in Section 4.6.3

$$V_{3B} = \sum_{C\neq E} GM_C[\frac{1}{r_{SC}} - \frac{1}{r_{EC}} + \frac{\mathbf{r}_{EC}\cdot\mathbf{r}_{SE}}{r_{EC}^3}] \tag{26}$$

4 RESULTS AND DISCUSSION

4.1 Clock Profiles

Simulated Allan deviation curves for four oscillators are presented in Figure 10. The CSAC and RAFS clocks are both commercially available whereas the ACES and ORAFS clocks are still experimental. This plot is used as a guideline for selecting an oscillator for the simulated constellation as well as to understand what type of time and frequency transfer requirements may be required for next generation space clocks.

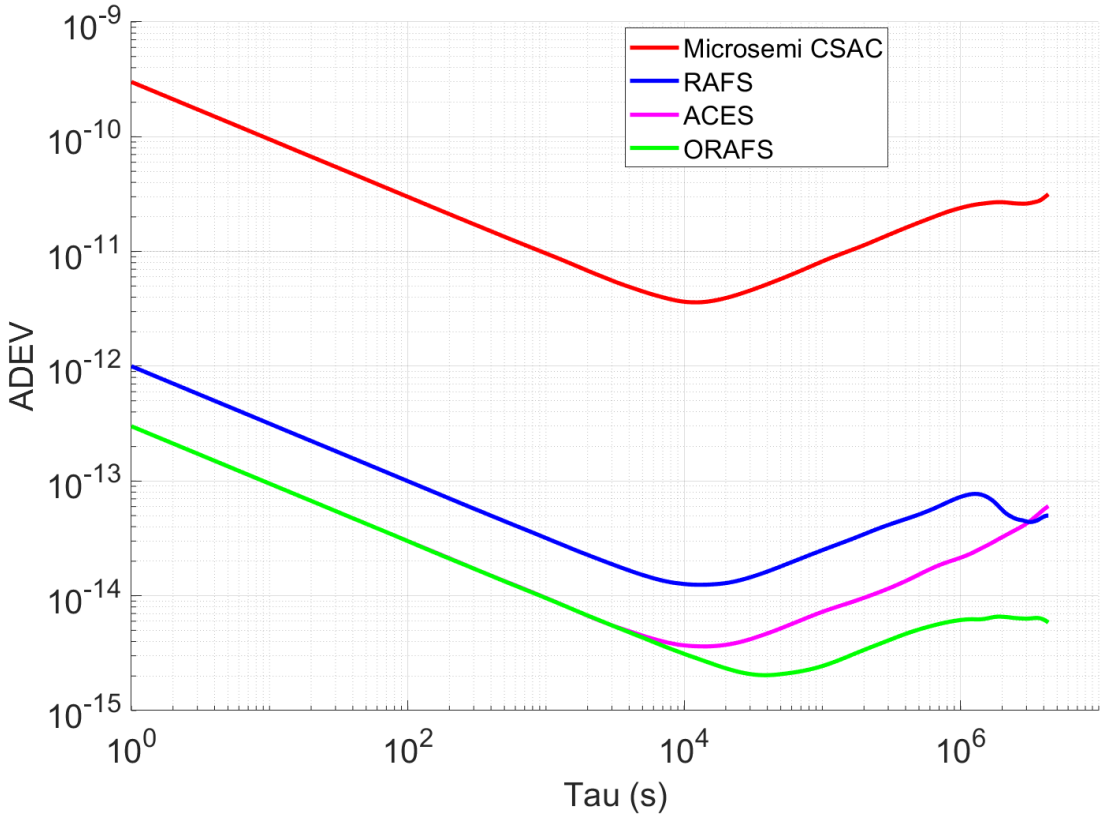

Figure 10. OADEVs of Various Simulated Clocks

Here we choose a rubidium atomic frequency standard (RAFS) as the simulated oscillator on each spacecraft. This clock has years of spaceflight heritage on GPS satellites [48] and recent trends [49] in atomic clock development suggest a low-SWaP clock with RAFS-like performance could fly on a small satellite in the next few years. The simulated behavior of 20 RAFS oscillators is shown in Figure 11. After this 24 hour simulation all of the clocks are within ±4 nanoseconds of true time. The corresponding Allan deviation curves are shown in Figure 12, along with the RAFS stability specifications.

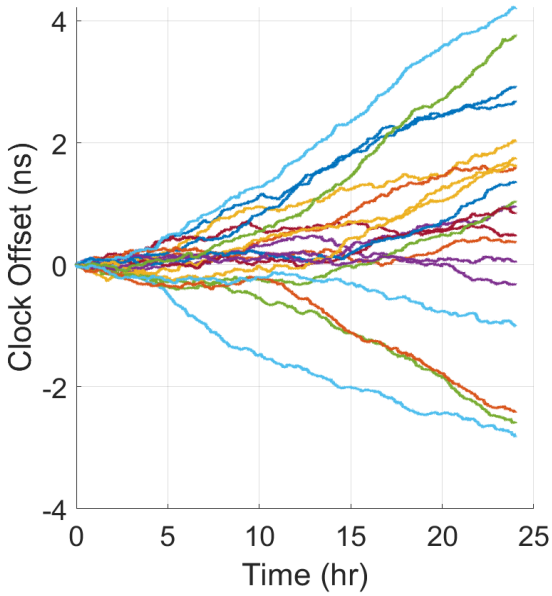

Figure 11. Simulated RAFS Time Series

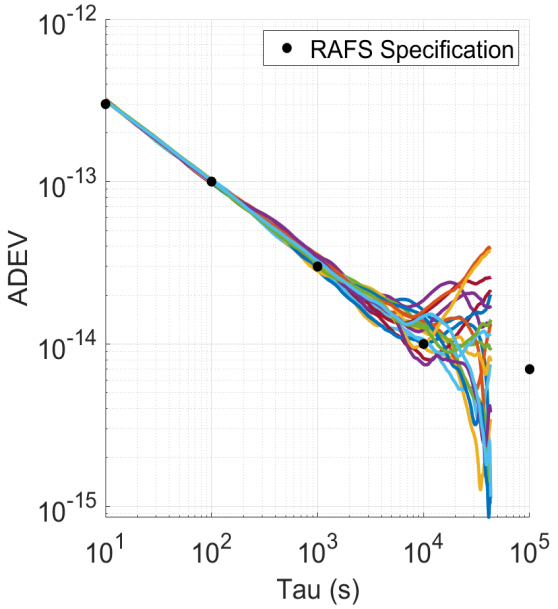

Figure 12. ADEV of Simulated RAFS

4.2 Satellite Constellations

The constellations described in Section 3.5 are each used in a separate estimation scenario. The Transport Layer constellation is used for just clock state estimation whereas the smaller, Blackjack Pit Boss constellation is used for clock state estimation and orbit determination. Visualizations of each constellation in GMAT are shown in Figure 13 and 14 below.

4.2.1 Transport Layer

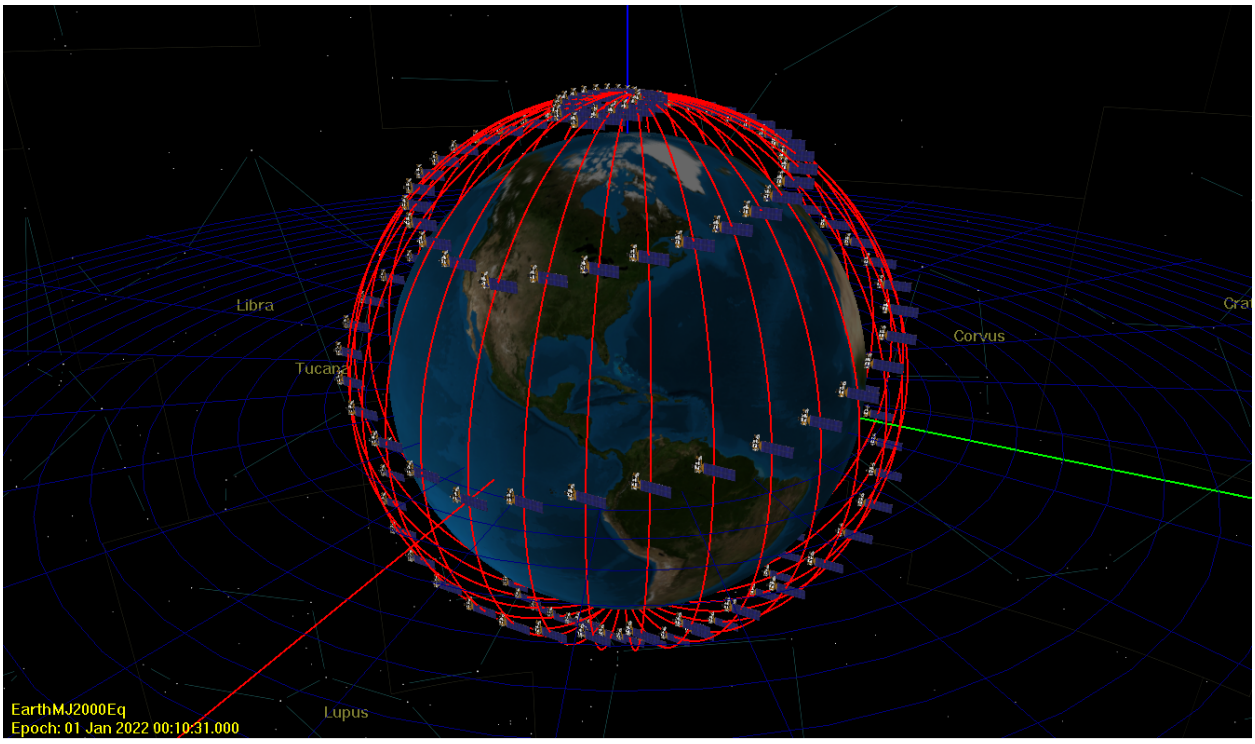

Figure 13. Simulated Transport Layer Constellation

4.2.2 Blackjack Pit Boss

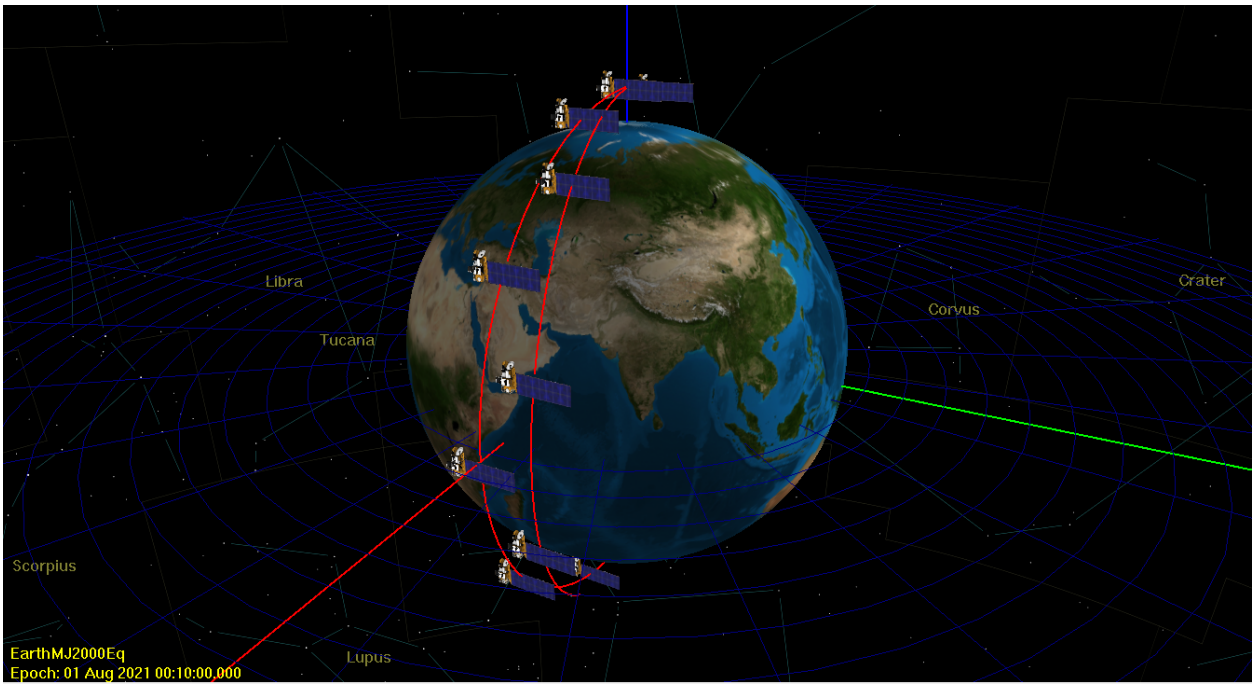

Figure 14. Simulated Blackjack Constellation

4.3 Two-Way Inter-satellite Range Models

The inter-satellite range between two satellites is computed using the methods described in Section 3.7. This section shows examples of inter-satellite range in the 20 satellite constellation from Section 4.2.2. In this configuration there are three categories of inter-satellite links: 1) links to the GEO satellite, 2) links to in-plane satellites, and 3) links to satellites in the adjacent plane. The measurements are computed with and without boresight angle restrictions to demonstrate the impact of sensor visibility on the number of available measurements.

4.3.1 Range to GEO

As a result of the geometry between the LEO and GEO satellites, all simulated optical terminals can produce range measurements. Examples of range measurements are shown in Figure 15. The magnitude of the range measurements can vary by as much as 10,000 kilometers depending on the orbit geometry.

The impact of implementing off-boresight restrictions on the LEO-GEO links is demonstrated by the red curves overlaid on top of the blue. With the restriction in place, the

number of measurement opportunities decreases significantly, which will ultimately affect estimation performance.

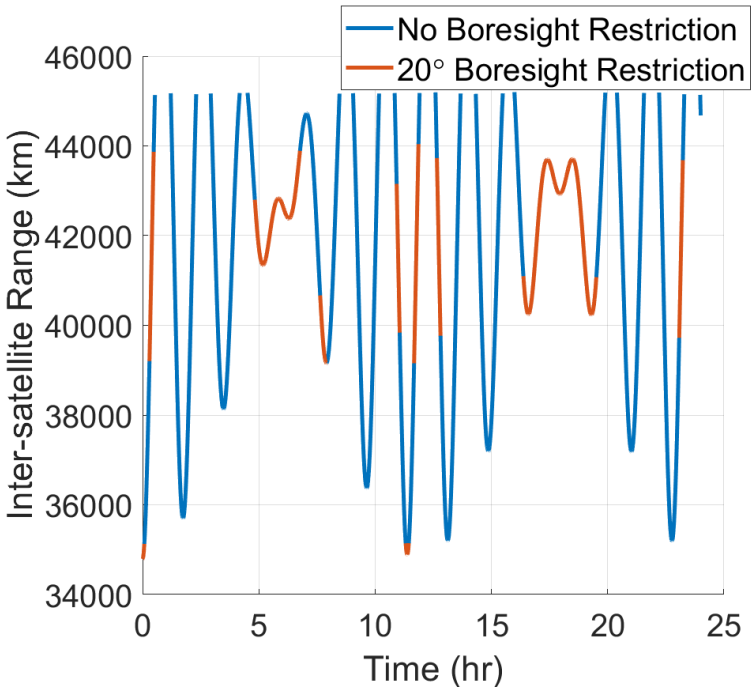

Figure 15. Simulated Inter-satellite Range from LEO to GEO

4.3.2 Range to LEO

Range measurements between LEO satellites in the same plane are shown in Figure 16. Referring back to the constellation geometry in Figure 4.2.2, we expect all LEO satellites to have a continuous, low dynamic link with the satellite ahead and behind in the same plane. We can see in the figure below that the distance between satellites in the same plane has a strong constant trend with superimposed oscillations due to the non-uniformity of Earth's geopotential. There is no change in the number of measurements when implementing off-boresight angle restrictions.

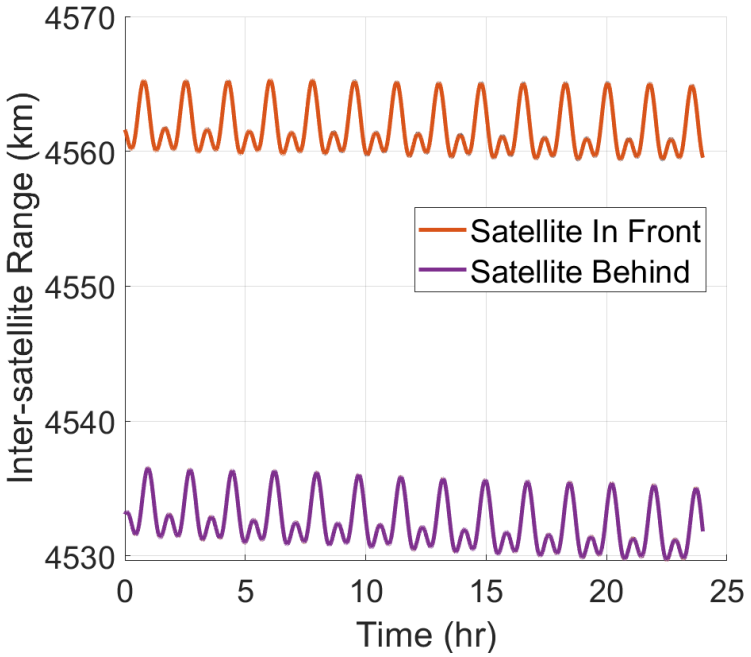

Figure 16. Simulated Inter-satellite Range from LEO to LEO - In-Plane

Figure 17 shows range measurements between satellites in adjacent planes. With no boresight restriction, the range between satellites has a strong sinusoidal trend due to planar crossings near the poles. An off-boresight restriction significantly reduces the number of available measurements to the planar crossings when the in-track sensors are closely aligned.

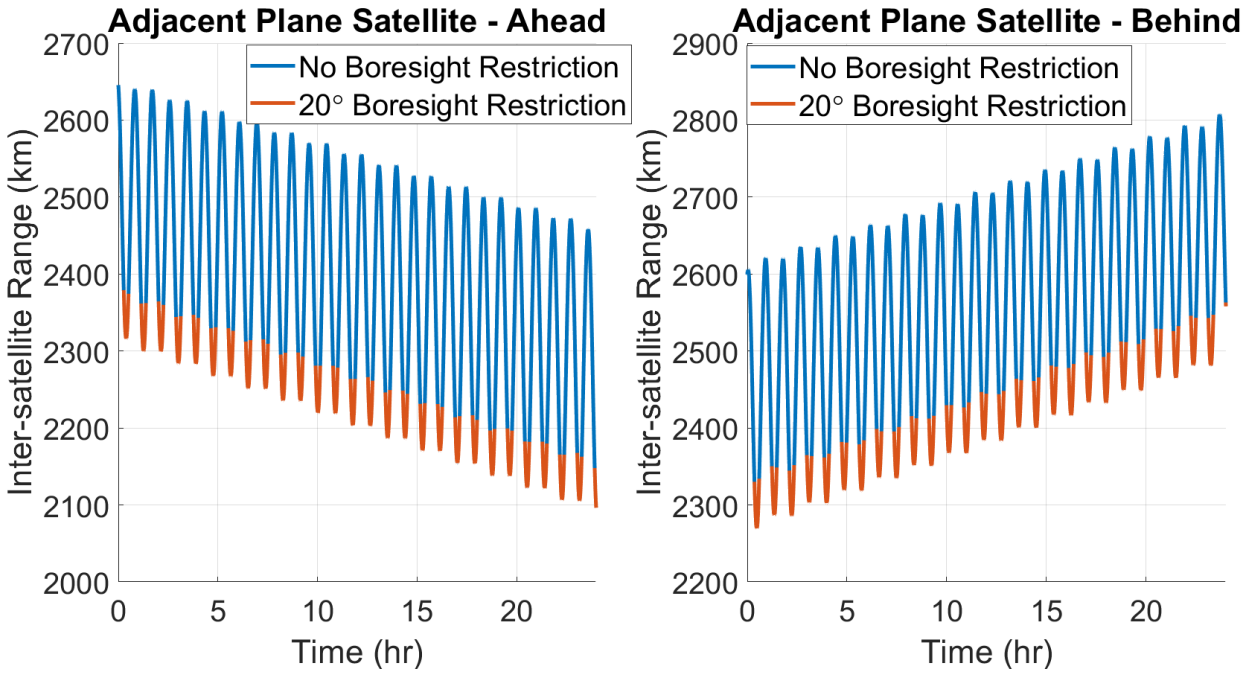

Figure 17. Simulated Inter-satellite Range from LEO to LEO - Cross-Plane

4.4 Clock State Estimation

We consider 12 unique scenarios with the possible measurement rates (1, 10, and 60 seconds), measurement noise values (30 and 100 picoseconds), and estimation methods (centralized and decentralized). Examples of the clock offset error results are shown in Figure 18 and Figure 19 for a single satellite.

4.4.1 Centralized

Figure 18 shows the clock offset error for a single satellite with a centralized estimation architecture with different measurement rates and measurement noise values. As the measurement noise and time between measurements increases, the clock offset error and uncertainty grow larger. The change from (a) to (b) is small due to the short measurement interval of 1 second. In (c) and (d) the clock offset uncertainty grows between measurements and creates a "saw tooth" pattern. The effect of the increase in measurement noise from Fig. (c) to (d) is more pronounced as a result of the longer measurement interval of one observation per minute.

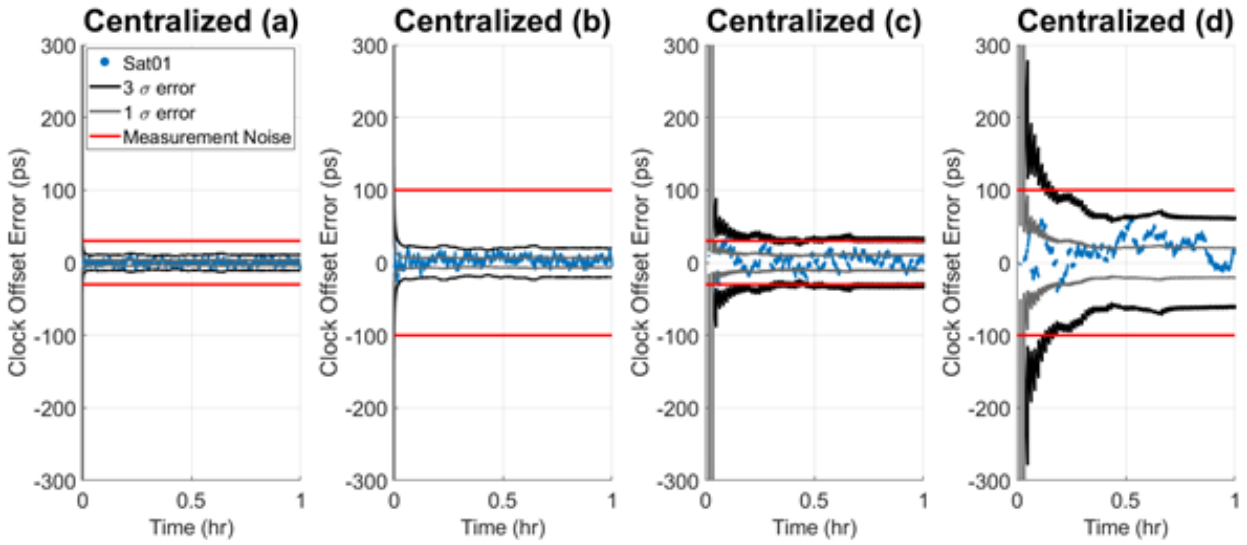

Figure 18. Time transfer error for a single satellite using a centralized estimation architecture. ***From left to right: a) 1s measurement rate, 30ps noise b) 1s measurement rate, 100ps noise, c) 60s measurement rate, 30ps noise, d) 60s measurement rate, 100ps noise***

4.4.2 Decentralized

In the decentralized estimation architecture each satellite has an estimated clock state history for the entire constellation; however, only the measurements made by the satellite are used directly and all other clock information converges through fusion of the shared estimates.

Figure 19 shows the clock offset error for the same satellite in Figure 18, but using decentralized estimation methods. As the measurement noise and time between measurements increase, the clock estimation quality decreases.

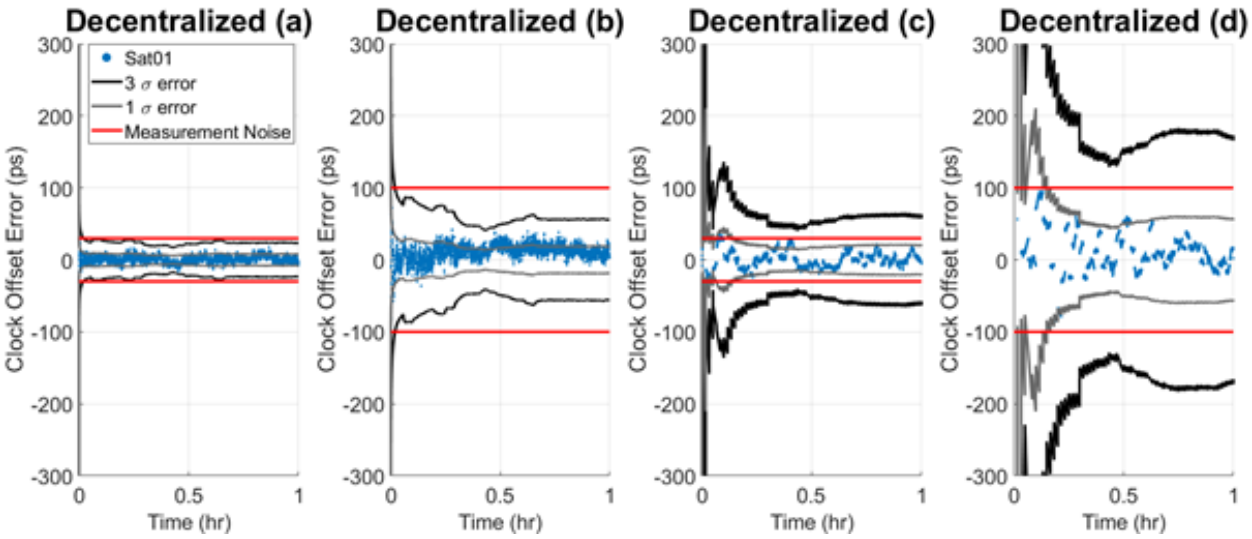

Figure 19: Time transfer error for a single satellite using a decentralized estimation architecture. ***From left to right: a) 1s measurement rate, 30ps noise b) 1s measurement rate, 100ps noise, c) 60s measurement rate, 30ps noise, d) 60s measurement rate, 100ps noise***

4.5 Orbit Determination & Clock State Estimation

Orbit determination was performed with and without off-boresight angle restrictions and for two measurement noise levels. The relationship between satellite geometry and estimation error is apparent in the position and velocity components, but not so much in the clock states. In all estimation results the state uncertainty is at a minimum when range to the GEO satellite is primarily along that axis. The estimation results yield position errors of 5 meters, velocity errors of 0.25 $\frac{m}{s}$, and clock offset errors of 50 picoseconds.

4.5.1 Hemispherical FOV: 90° Off-Boresight

Without restrictions on sensor visibility there are a large number of measurements, resulting in optimistic estimation errors. The increase in measurement noise from Figure 20 to Figure 21 has minimal impact on state error due to the number of available measurements.

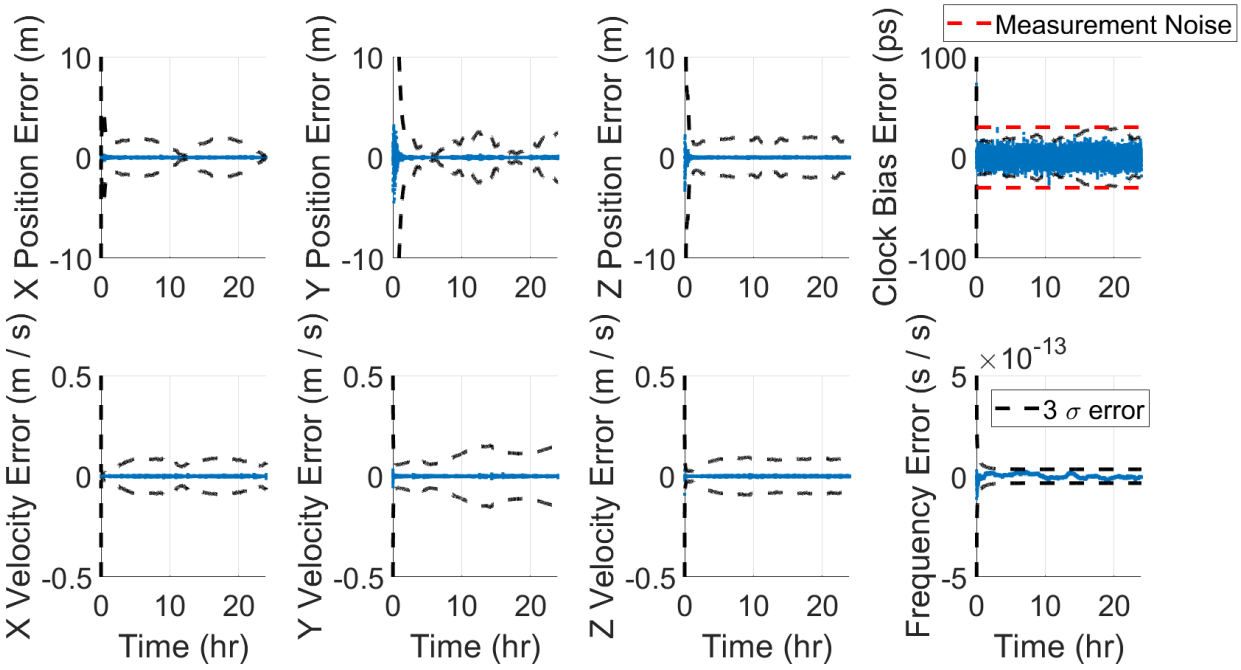

Figure 20. Orbit Determination Results with 30ps Measurement Noise

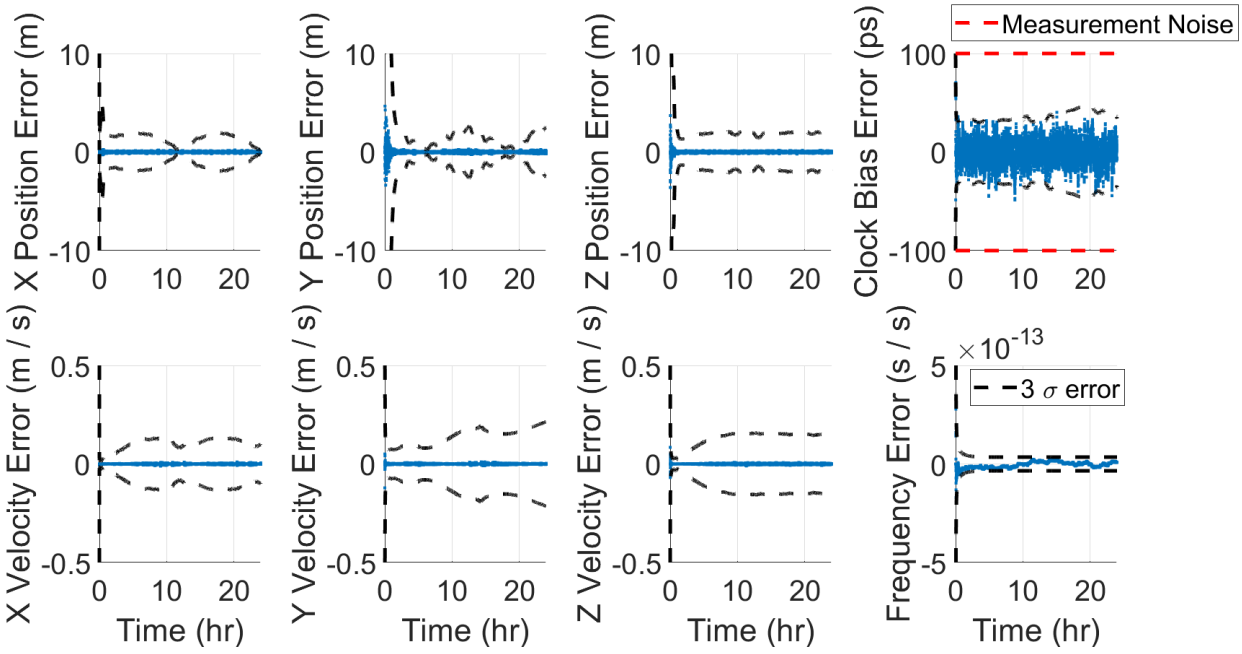

Figure 21. Orbit Determination Results with 100ps Measurement Noise

4.5.2 FOV Limited to 20° Off-Boresight

With off-boresight angle restrictions in place, the number of viable measurements is significantly reduced. There is now a clear degradation in the results shown in Figure 20,21 as compared to 22,23. All uncertainties are larger and the clock offset uncertainty has a sawtooth pattern, indicating periods of time where measurements to the GEO satellite are unavailable.

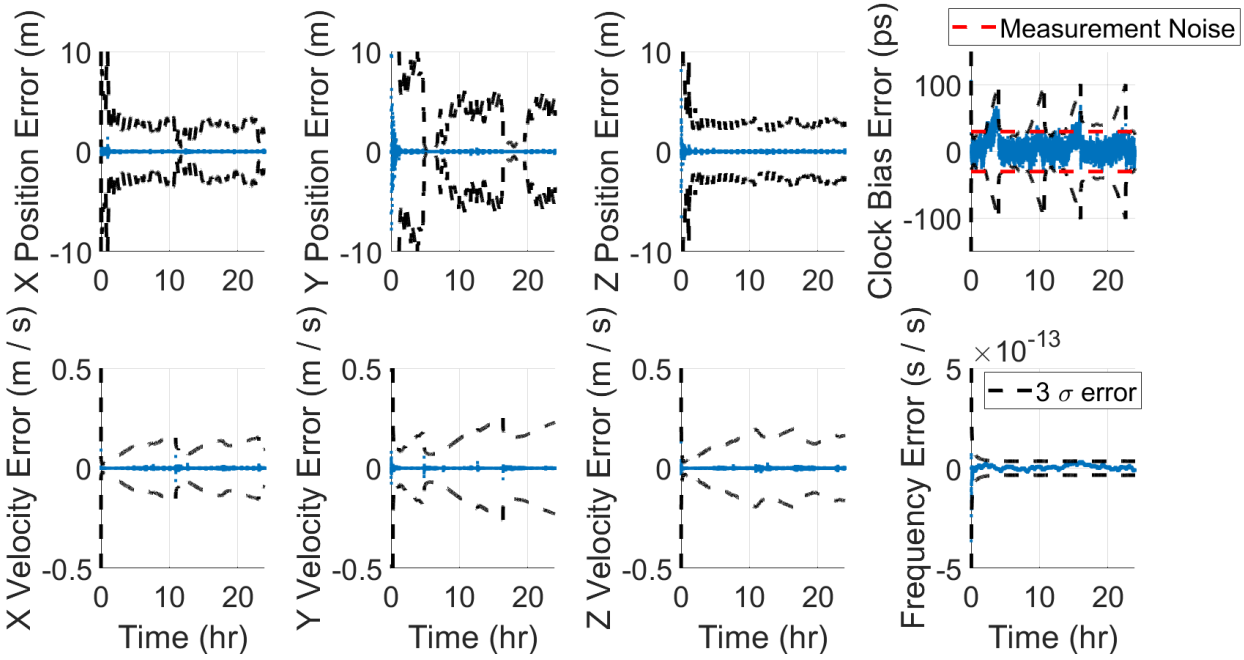

Figure 22. Orbit Determination Results with 30ps Measurement Noise, Limited Boresight

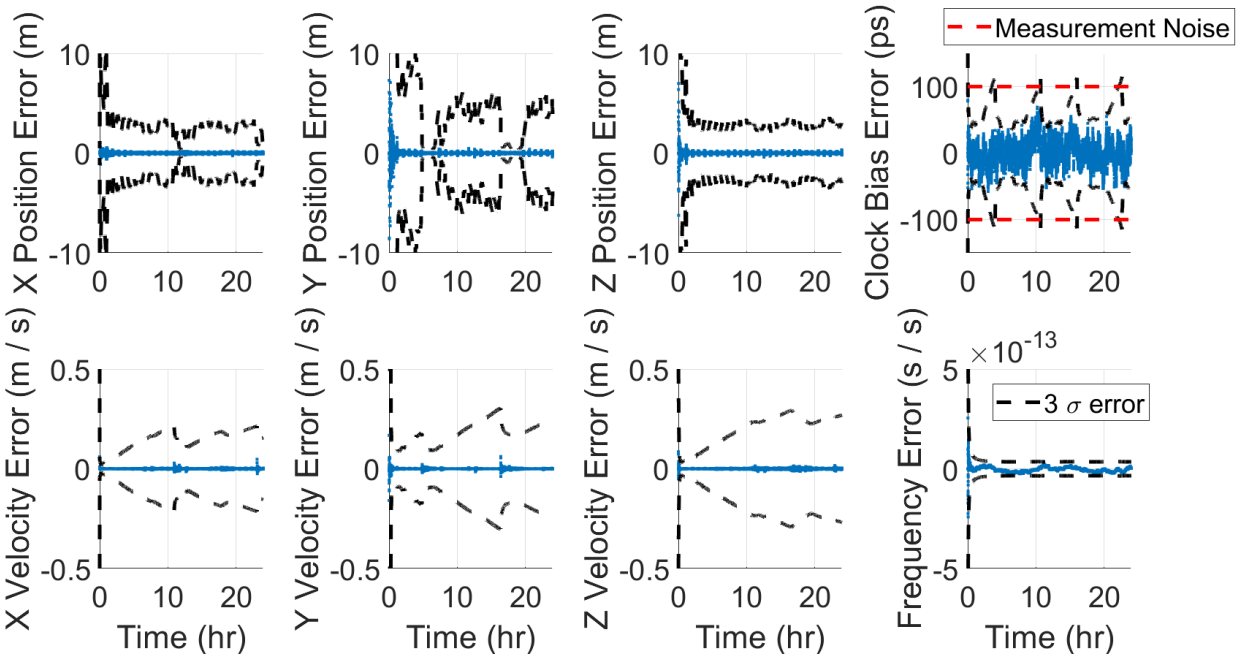

Figure 23. Orbit Determination Results with 100ps Measurement Noise, Limited Boresight

4.6 Relativistic Effects on Time & Frequency Transfer

4.6.1 Relative Velocity

The velocity induced frequency shift as measured in an inertial reference frame is shown in Figure 24. The magnitude of the effect is comparable to the frequency shift from Earth's center of mass, represented by the data point at spherical harmonic degree 1 in Figure 25.

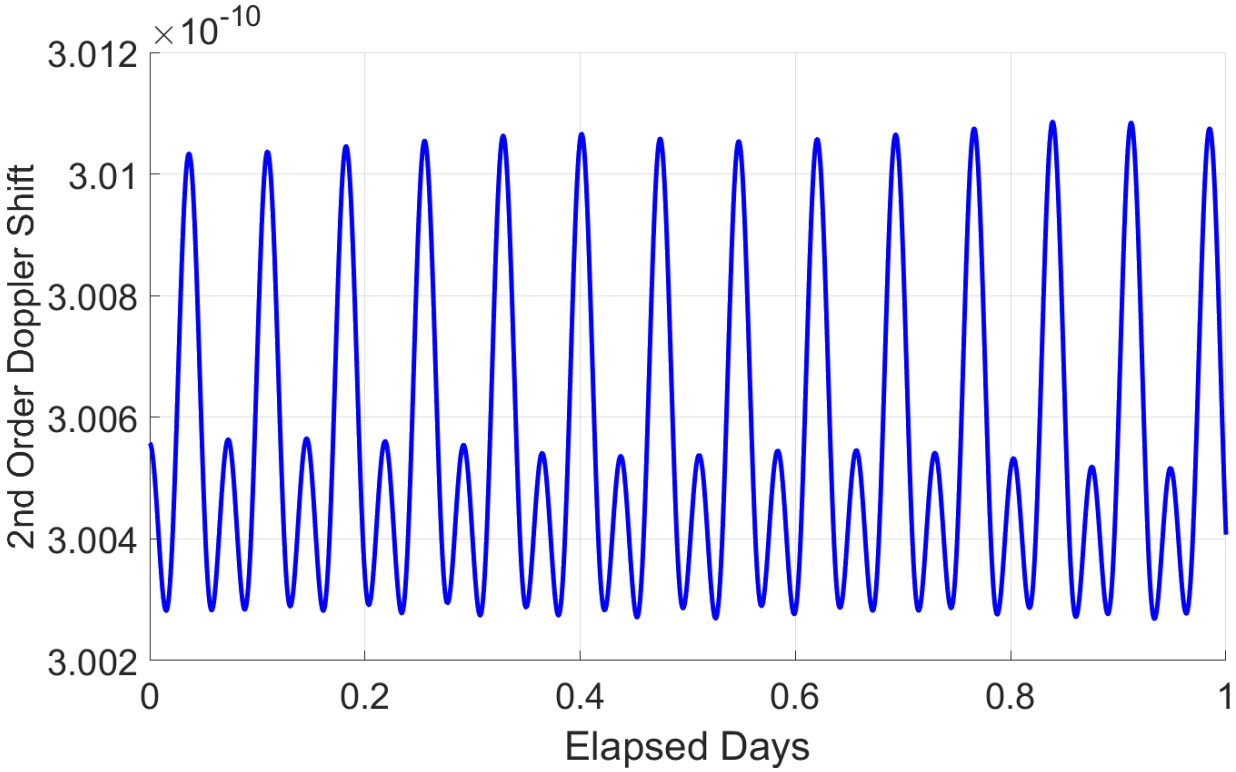

Figure 24. Second Order Doppler for LEO Satellite

4.6.2 Earth's Geopotential

The maximum absolute contribution for each degree of the Earth's gravity field is shown in Figure 25. The largest contributions are from the Earth's center of mass and J_2, after which the next largest frequency shift is 10^{-15}. This plot can be used to determine how high fidelity of a geopotential is required to achieve a certain frequency transfer accuracy. The most stable clock in Figure 10 has a minimum frequency stability of 10^{-15} corresponding to a modelling requirement of Earth's gravity field up to degree 3. Next generation clocks may have frequency stability on the order of 10^{-18}, which would require modeling of Earth's gravity field up to around degree 30.

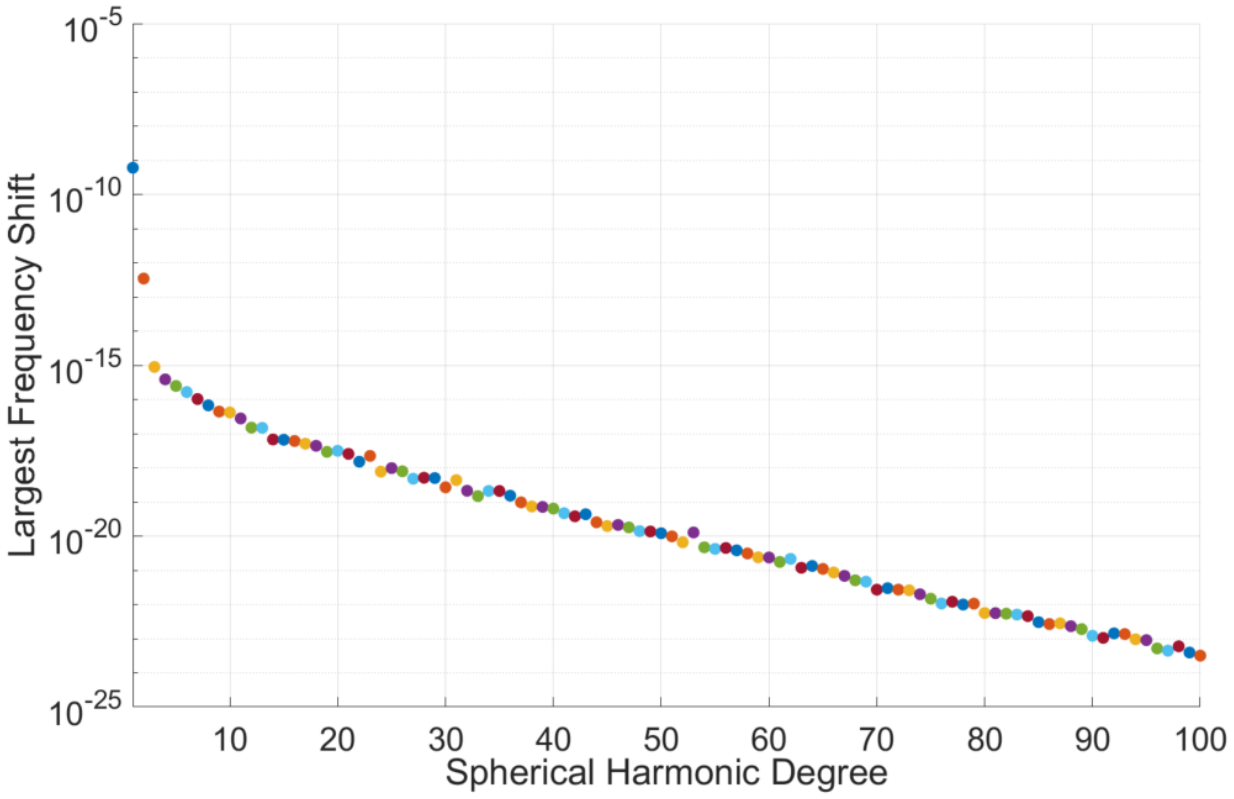

Figure 25. Frequency Shift due to Earth Geopotential

4.6.3 Celestial Bodies

The gravitational potential from third bodies in the solar system results in small, but non-negligible effects on observed oscillator frequency. Figure 26 shows the frequency shift of an oscillator in LEO due to various third bodies. None of the contributions are at the 10^{-15} level, but clocks with frequency stability below 10^{-17} will need to at least consider the Sun and Moon. The magnitude of the frequency shift is orbit dependent and would need to be reevaluated for higher orbits or orbits around the Moon.

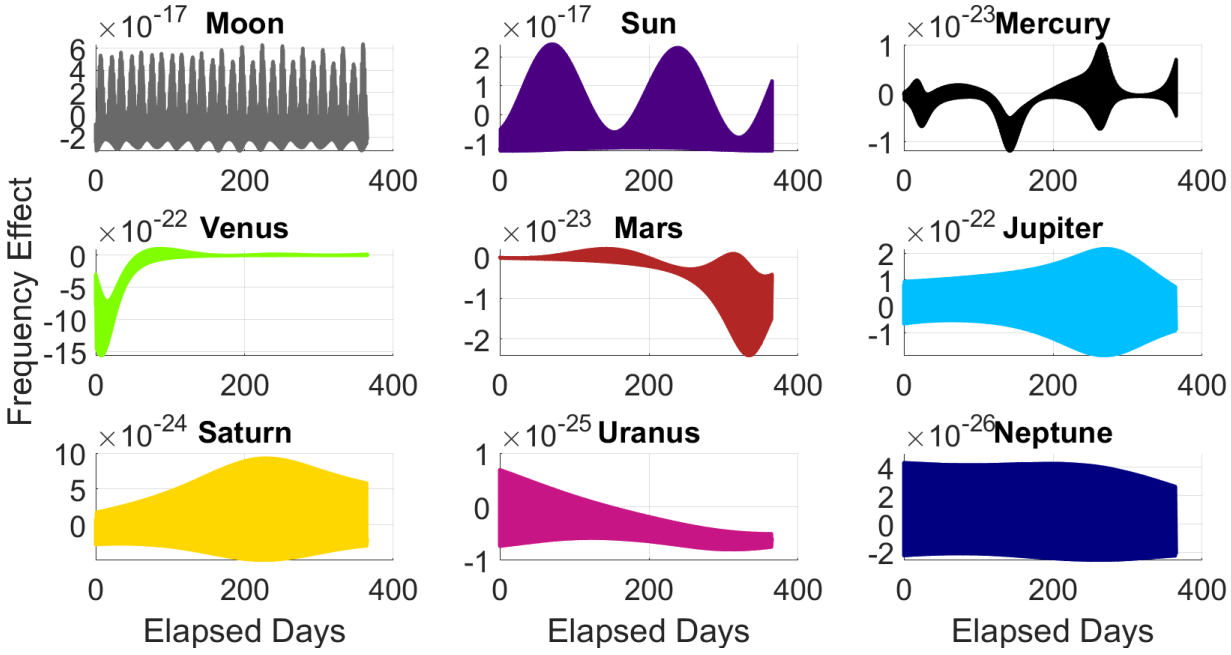

Figure 26. Third Body Effects on Oscillator in LEO

5 CONCLUSIONS

In this work we presented an analysis of two-way ranging measurements as the basis for a time transfer architecture between satellites in LEO constellations. Research into precise, low-SWaP, space-qualified time transfer techniques is motivated by current limitations in comparing next-generation clocks due to noisy time transfer methods. We showed in simulation that based on an assumption of constellation connectivity, compact optical terminals being developed for inter-satellite communication could be used to make ranging measurements in support of both time transfer and orbit determination. Key performance limitations are a small terminal field of view limiting the number of measurements, magnitude of the measurement noise, and the measurement rate.

Two estimation architectures were presented in Section 4.4, centralized and decentralized. Centralized estimation methods provide the smallest clock offset error, but impose potentially significant communication requirements that scale poorly with increasing constellation size. The decentralized estimation method results in increased clock errors, but is a more practical method to implement that scales better with a growing number of participants. Section 4.5 used inter-satellite range measurements for orbit determination in addition to clock state estimation, as applied to a similar satellite constellation. There is a strong correlation between the GEO satellite geometry and estimated position / velocity of the satellite, whereas the clock estimates are not correlated to the geometry.

With high-stability clocks the effects of relativity are non-negligible. A brief analysis of Earth's geopotential, potential contribution of third bodies, and spacecraft velocity showed the magnitude of the effects with respect to an inertial coordinate frame. The stability of a RAFS clock in LEO would require modeling of the geopotential up to degree 3 and the second order Doppler contribution. Clocks with better stability or in higher orbits may need to consider the effect of the Sun and Moon. The frequency shifts and corresponding impact on the clock state estimation were not modeled here but will be incorporated in future work.

To date, simulation of inter-satellite ranging and time transfer has been primarily based on models from existing literature. Future work will include collaborating with other labs in the area, primarily NIST, to generate data with optical hardware. Additionally, the relativistic analysis presented in [39] and [40] will be applied to the LEO constellations presented here to determine the orbit knowledge requirements for inter-satellite two-way time and frequency transfer. The relativistic analysis could extend to other orbit regimes, such as in GEO or in cis-lunar space.

REFERENCES

[1] I. Khader, H. Bergeron, L. C. Sinclair, W. C. Swann, N. R. Newbury, and J.-D. Deschênes, "Time synchronization over a free-space optical communication channel," *Optica*, vol. 5, no. 12, pp. 1542–1548, Dec. 2018.

[2] B. D. Tapley, B. E. Schutz, and R. Eanes, "Satellite laser ranging and its applications," *Celestial Mechanics*, vol. 37, pp. 247–261, 1985.

[3] D. M. Boroson, *et al.*, "Overview and results of the Lunar Laser Communication Demonstration," in *Free-Space Laser Communication and Atmospheric Propagation XXVI*, H. Hemmati and D. M. Boroson, Eds., International Society for Optics and Photonics, vol. 8971, SPIE, 2014, 89710S.

[4] P. Guillemot, P. Exertier, E. Samain, F. Pierron, J.-M. Torre, and S. Leon, "Time Transfer by Laser Link-T2L2: Results of the First Year of Operation," *41st Annual Precise Time and Time Interval (PTTI) Systems and Applications Meeting 2009*, Jan. 2009.

[5] J. C. McDowell, "The Low Earth Orbit Satellite Population and Impacts of the SpaceX Starlink Constellation," *The Astrophysical Journal*, vol. 892, no. 2, p. L36, Apr. 2020.

[6] F. Heine, *et al.*, "Status of Tesat laser communication activities," in *Free-Space Laser Communications XXXII*, H. Hemmati and D. M. Boroson, Eds., International Society for Optics and Photonics, vol. 11272, SPIE, 2020, p. 1 127 204.

[7] R. W. Kingsbury, J. C. Twichell, and S. E. Palo, "Cobalt optical crosslink terminal," in *Free-Space Laser Communications XXXIV*, H. Hemmati and B. S. Robinson, Eds., International Society for Optics and Photonics, vol. 11993, SPIE, 2022, 119930N.

[8] A. D. Ludlow, M. M. Boyd, J. Ye, E. Peik, and P. O. Schmidt, "Optical atomic clocks," *Rev. Mod. Phys.*, vol. 87, pp. 637–701, 2 Jun. 2015.

[9] W. Lewandowski, J. Azoubib, and W. Klepczynski, "GPS: primary tool for time transfer," *Proceedings of the IEEE*, vol. 87, no. 1, pp. 163–172, 1999.

[10] P. Exertier *et al.*, "Sub-ns time transfer consistency: A direct comparison between GPS CV and T2L2," *Metrologia*, vol. 53, pp. 1395–1401, Dec. 2016.

[11] P. Fridelance and C. Veillet, "Operation and data analysis in the LASSO experiment," *Metrologia*, vol. 32, no. 1, pp. 27–33, Jan. 1995.

[12] K. Larson and J. Levine, "Carrier-phase time transfer," *IEEE Transactions on Ultrasonics, Ferroelectrics, and Frequency Control*, vol. 46, no. 4, pp. 1001–1012, 1999.

[13] G. Petit and P. Defraigne, "The performance of GPS time and frequency transfer: Comment on 'A detailed comparison of two continuous GPS carrier-phase time transfer techniques'," *Metrologia*, vol. 53, pp. 1003–1008, Jun. 2016.

[14] V. Zhang, *et al.*, "Two-Way Satellite Time and Frequency Transfer Using 1 MChips/s Codes," Nov. 2009.

[15] R. Emardson, *et al.*, "Time Transfer by Passive Listening Over a 10Gb/s Optical Fiber," *IEEE Transactions on Instrumentation and Measurement*, vol. 57, pp. 2495–2501, Nov. 2008.

[16] P. Exertier, *et al.*, "Time Transfer by Laser Link: Data analysis and validation to the ps level," *Advances in Space Research*, vol. 54, no. 11, pp. 2371–2385, 2014.

[17] J. Savory, J. Sherman, and S. Romisch, "White Rabbit-Based Time Distribution at NIST," in *2018 IEEE International Frequency Control Symposium (IFCS)*, 2018, pp. 1–5.

[18] J. D. Deschênes, *et al.*, "Synchronization of Distant Optical Clocks at the Femtosecond Level," *Phys. Rev. X*, vol. 6, p. 021 016, 2 May 2016.

[19] B. Baumgartner, C. Riesch, and W. Schenk, "The impact of GPS vulnerabilities on the electric power grid," in *XX IMEKO World Symposium*, 2014, pp. 183–188.

[20] P. Misra and P. Enge, *Global Positioning System: Signals, measurements, and performance*. Ganga-Jamuna Press, 2012.

[21] *The operational use of two-way satellite time and frequency transfer employing pseudorandom noise codes*, Aug. 2015.

[22] T. von Lerber, S. Honkanen, A. Tervonen, H. Ludvigsen, and F. Küppers, "Optical clock recovery methods: Review," *Optical Fiber Technology*, vol. 15, no. 4, pp. 363–372, 2009.

[23] P. Fridelance, E. Samain, and C. Veillet, "T2L2 - Time transfer by Laser link: a new optical time transfer generation," *Experimental Astronomy*, vol. 7, pp. 191–207, 1997.

[24] J. Serrano, *et al.*, "The White Rabbit Project," Nov. 2009.

[25] B. D. Tapley, S. Bettadpur, M. Watkins, and C. Reigber, "The gravity recovery and climate experiment: Mission overview and early results," *Geophysical Research Letters*, vol. 31, no. 9, 2004.

[26] K. Abich, *et al.*, "In-Orbit Performance of the GRACE Follow-on Laser Ranging Inter-ferometer," *Phys. Rev. Lett.*, vol. 123, p. 031 101, 3 Jul. 2019.

[27] M. T. Zuber, *et al.*, "Gravity Field of the Moon from the Gravity Recovery and Interior Laboratory (GRAIL) Mission," *Science*, vol. 339, no. 6120, pp. 668–671, 2013.

[28] W. M. Klipstein, *et al.*, "The Lunar Gravity Ranging System for the Gravity Recovery and Interior Laboratory (GRAIL) Mission," in *GRAIL: Mapping the Moon's Interior*. New York, NY: Springer New York, 2014, pp. 57–76.

[29] C. Zucca and P. Tavella, "The clock model and its relationship with the Allan and related variances," *IEEE Transactions on Ultrasonics, Ferroelectrics, and Frequency Control*, vol. 52, no. 2, pp. 289–296, 2005.

[30] W. Riley and D. Howe, *Handbook of Frequency Stability Analysis*, 2008-07-01 00:07:00 2008.

[31] D. Allan, "Statistics of atomic frequency standards," *Proceedings of the IEEE*, vol. 54, no. 2, pp. 221–230, 1966.

[32] *Broad Agency Announcement: Blackjack Pit Boss*, en, 2019.

[33] T. Boudreaux, *SDA: Transport Tranche 0 Overview*, 2020.

[34] S. Hughes, "General Mission Analysis Tool (GMAT)," *International Conference of Astrodynamics Tools and Techniques*, 2016.

[35] P. Exertier, *et al.*, "Time and laser ranging: a window of opportunity for geodesy, navigation, and metrology," *Journal of Geodesy*, vol. 93, Jul. 2018.

[36] K. Schreiber and J. Kodet, "The Application of Coherent Local Time for Optical Time Transfer and the Quantification of Systematic Errors in Satellite Laser Ranging," *Space Science Reviews*, vol. 214, Dec. 2017.

[37] E. Samain, *et al.*, "Time transfer by laser link: A complete analysis of the uncertainty budget," *Metrologia*, vol. 52, Apr. 2015.

[38] S. Julier and J. Uhlmann, "General Decentralized Data Fusion with Covariance Intersection (CI)," in Jun. 2001.

[39] L. Duchayne, F. Mercier, and P. Wolf, "Orbit determination for next generation space clocks," *Astronomy and Astrophysics*, vol. 504, pp. 653–661, 2007.

[40] B. Kroese, G. Giorgi, and C. Günther, "Relativistic corrections for intersatellite frequency transfer," in *2018 European Frequency and Time Forum (EFTF)*, 2018, pp. 240–244.

[41] W. Isaacson, *Einstein: His life and universe*, Simon & Schuster, 2008.

[42] A. Einstein, "Zur Elektrodynamik bewegter Körper," *Annalen der Physik*, vol. 322, no. 10, pp. 891–921, 1905.

[43] R. Wolfson and J. M. Pasachoff, *Physics for scientists and engineers*. HarperCollins, 1995.

[44] A. Einstein, "Über das Relativitätsprinzip und die aus demselben gezogenen Folgerungen," *Jahrbuch der Radioaktivität und Elektronik*, vol. 4, pp. 411–462, 1907.

[45] J. Wahr, S. Swenson, V. Zlotnicki, and I. Velicogna, "Time-variable gravity from GRACE: First results," *Geophysical Research Letters*, vol. 31, no. 11, 2004.

[46] M. van der Meijde, R. Pail, R. Bingham, and R. Floberghagen, "GOCE data, models, and applications: A review," *International Journal of Applied Earth Observation and Geoinformation*, vol. 35, pp. 4–15, 2015.

[47] F. Flechtner, P. Morton, M. Watkins, and F. Webb, "Status of the GRACE Follow-On Mission," in *Gravity, Geoid and Height Systems*, U. Marti, Ed., Cham: Springer International Publishing, 2014, pp. 117–121.

[48] B. Jaduszliwer and J. Camparo, "Past, present and future of atomic clocks for GNSS," *GPS Solutions*, vol. 25, Jan. 2021.

[49] D. Scherer, "The Future of Industrial Atomic Clocks," *Proceedings of the 53rd Annual Precise Time and Time Interval Systems and Applications Meeting*, pp. 18–42, Jan. 2022.

DISTRIBUTION LIST

DTIC/OCP
8725 John J. Kingman Rd, Suite 0944
Ft Belvoir, VA 22060-6218 1 cy

AFRL/RVIL
Kirtland AFB, NM 87117-5776 1 cy

Official Record Copy
AFRL/RVB/Dr. Spencer E.Olson 1 cy